RADIATIVE AND TRANSIENT THERMAL MODELING OF SOLID OXIDE FUEL CELLS

A Thesis
Presented to
The Academic Faculty

by

David Lee Damm

In Partial Fulfillment
Of the Requirements for the Degree
Master of Science in the
School of Mechanical Engineering

Georgia Institute of Technology

December 2005

RADIATIVE AND TRANSIENT THERMAL MODELING OF SOLID OXIDE FUEL CELLS

Approved by:

Dr. Andrei G. Fedorov, Advisor
School of Mechanical Engineering
Georgia Institute of Technology

Dr. Jianmin Qu
School of Mechanical Engineering
Georgia Institute of Technology

Dr. Samuel Graham
School of Mechanical Engineering
Georgia Institute of Technology

Date Approved: November 15, 2005

In general, after having established the fundamental equations of movement of heat, and the method of calculation which serves to integrate them, I turned to the solutions of the questions…and made known the relations of this study to the systematic behavior of the world.

-*Jean-Baptiste Joseph Fourier* [1]

ACKNOWLEDGEMENTS

It would be inappropriate to proceed without giving credit where credit is due:

-money

This project was funded by the U.S. Department of Energy's Solid State Energy Conversion Alliance (SECA) program. Personally, I also received funding from the U.S. Department of Defense through the National Defense Science and Engineering Graduate Fellowship program. These supporting agencies are hereby acknowledged and greatly appreciated.

-planning

My advisor, Dr. Andrei G. Fedorov did an excellent job in defining the content and scope of the research (as appropriate for Masters level work), and creating a realistic timeline with milestones to keep me focused. Also, thanks go out to Dr. Sunil Murthy who, as a graduate student researcher, assisted me in the transition from his work, Phase I of the SECA project, to my own work described here in Phase II.

-inspiration and perspiration

First, I thank God for giving me a brain that works. Second, I thank Dr. Fedorov for teaching, advising, encouraging, and inspiring me to achieve. Finally, I thank my parents for the many sacrifices they made for me; I know that I often merely reap the rewards of their hard work. And without the values they taught me, I surely would have wasted these gifts.

TABLE OF CONTENTS

LIST OF TABLES

LIST OF FIGURES

LIST OF SYMBOLS

a_s specific surface area [m^{-1}]
c_p specific heat [$J\ kg^{-1}K^{-1}$]
$E_{b\lambda}$ blackbody emissive power [$W\ m^{-2}\ \mu m^{-1}$]
h convective heat transfer coefficient [$Wm^{-2}K^{-1}$]
H_o incident radiation [$W\ m^{-2}\ \mu m^{-1}$]
i current density [$A\ m^{-2}$]
I_λ spectral intensity of radiation [$W\ m^{-2}\ \mu m^{-1}$]
k thermal conductivity [$Wm^{-1}K^{-1}$]
K rate of inlet temperature rise [$°C\ s^{-1}$]
K_{eff} dimensionless (effective) rate of inlet temperature rise
n refractive index of medium
q_λ spectral radiative heat flux [$W\ m^{-2}\ \mu m^{-1}$]
q_r total radiative heat flux [$W\ m^{-2}$]
Pe effective Peclet number of the flow, $u_{eff} L / \alpha_{eff}$
T_f final (operating) temperature [$°C$]
T_o initial temperature [$°C$]
Tr transmittance of medium
u velocity of air stream [$m\ s^{-1}$]

Greek Letters

α thermal diffusivity [$m^2 s^{-1}$]
β extinction coefficient [m^{-1}]
ε emissivity of boundary; or porosity of medium
κ absorption coefficient [m^{-1}]
λ wavelength [μm]
η kinematic viscosity [$m^2 s^{-1}$]
ρ reflectivity; or density [$kg\ m^{-3}$]
σ Stefan-Boltzmann constant [$J\ K^{-4}\ m^{-2}\ s^{-1}$]
σ_s scattering coefficient of medium
τ_h^* dimensionless total heating time
τ_c advective time scale [s]
τ_h total heating time [s]
τ_λ spectral optical thickness
τ_L total optical length of a medium
ω single scattering albedo
Φ scattering phase function

SUMMARY

Thermo-mechanical failure of components in planar-type solid oxide fuel cells (SOFCs) is a major obstacle on the path to bringing this technology to commercial viability. The probability of material degradation and failure in SOFCs depends strongly on the local temperature gradients at the interfaces of different materials. Therefore, it is of paramount importance to accurately predict and manage the temperature fields within the stack, especially near the interfaces. In this work we consider three effects in detail.

First, we analyze radiative heat transfer effects within the semi-transparent solid electrolyte and compared them to thermal conduction. We also, present the modeling approach for calculation of surface-to-surface exchange within the flow channels and from the stack to the environment. The simplifying assumptions are identified and their carefully justified range of applicability to the problem at hand is established. This allows thermal radiation effects to be properly included in overall thermal modeling efforts with the minimum computational expense requirement. The work reported in this chapter has recently been published in refereed journals [2, 3].

Second, we developed a series of reduced-order models for the transient heating and cooling of a cell, leading to a framework for optimization of these processes. The optimal design is one that minimizes heating time while maintaining thermal gradients below an allowable threshold. To this end, we formulated reduced order models (validated by rigorous CFD simulations) that yield simple algebraic design rules for predicting maximum thermal gradients and heating time requirements. Several governing dimensionless parameters and time scales were identified that shed light on the essential physics of the process. The contents of this chapter are currently under review for journal publication [4].

Finally, an analysis was performed to assess the degree of local thermal non-equilibrium (LTNE) within porous SOFC electrodes, and through a simple scaling analysis we discovered the parameter that gives an estimate of the magnitude of LTNE effects. We conclude that because of efficient heat transfer between the solid and gas in the microscale pores of the electrodes, the temperature difference between gas and solid is often negligible. However, if local variations in current density are significant, the LTNE effects may become significant and should be considered. The contents of this chapter are currently under review for journal publication [5].

CHAPTER 1

INTRODUCTION

Solid Oxide Fuel Cells (SOFCs) are power plants that produce electricity directly and in an environmentally benign way by electrochemically reacting hydrogen and oxygen. With the potential for very high efficiency (~70% anticipated by some manufacturers of hybrid SOFC-gas turbine systems) and zero emissions (water is the only reaction byproduct), they are an attractive alternative power source for the future. Several distinct advantages that they enjoy over other types of fuel cells arise from elevated operating temperatures (600 - 800 ^{o}C). These include 1) the use of nickel (rather than expensive precious metals such as platinum) as a catalyst, 2) the ability to internally reform fuels such as methane or other hydrocarbons, 3) tolerance of carbon monoxide, sulfur, and other contaminants in the fuel and oxidizer streams, and 4) high quality waste heat that can be recovered to increase overall thermodynamic efficiency of the power generation system. However, these benefits come at a cost—thermo-mechanically induced degradation and failure of the delicate anode-electrolyte-cathode (PEN) structure is a critical roadblock in bringing this technology to the point of commercial viability. Central to mitigation of this failure mode is the ability to accurately manage and predict thermal gradients within the cell, especially at the interface of the ultra-thin (15 μm or less) solid electrolyte and porous anode/cathode layers. Thus, thermal modeling of SOFCs has generated significant interest in recent years, resulting in highly detailed CFD and FEM based models that predict the coupled current density, flow, species, and temperature fields within a cell.

Several weaknesses and shortcomings of these state-of-the-art models are addressed in the current research. Chapter 2 considers the role of thermal radiation as a heat transfer mechanism in SOFC unit cells and stacks. A review of the literature in this area shows that few works consider its effect on the operating conditions of the cell, and those that do, consider it in a highly simplified fashion, often reporting conflicting results. The inherent complexity of radiative transfer models and the computational expense of calculating radiative heat flux and coupling it to the other modes of heat transfer are typical reasons for neglecting radiation. For this reason, the issue of thermal radiation in SOFCs, at both the component (unit cell) and system (stack) level, is addressed.

In Chapter 3 transient thermal models for simulating the startup and shutdown of SOFCs are considered. The need for fast and safe methods of bringing the cell from ambient temperature to the elevated temperature of steady state operation, or vise-versa, is currently an important issue to broadening the use of the SOFC especially in transportation applications. Although state of the art CFD or FEM models can potentially simulate this transient startup/shutdown behavior, they do so at a significant computational expense with highly complex models. To address this challenge, reduced order transient thermal models of varying complexity are developed and results are used to develop simple, accurate, and concise design rules for optimization of the transient process. This approach enables efficient parametric search of the design space during the early stages of conceptual development by providing a valuable industry tool for bringing SOFCs to market.

The fourth and final chapter of this thesis critically assesses the validity of one of the key assumptions of state-of-the-art SOFC modeling tools, that of local thermal equilibrium between the gas and solid matrix within the porous electrodes. A survey of the relevant

literature indicates that most (possibly all) of the current models make this assumption with little or no justification given. Here, a two-equation, thermal non-equilibrium model of heat transfer between the gas and solid phase and its scaling analysis are used to estimate the magnitude of the temperature difference that would be expected between the gas and solid phase, and thus the significance of local thermal non-equilibrium effects. A simple criterion based on this analysis is then developed for determining under what conditions local thermal non-equilibrium effects may safely be neglected, and when they are likely to become significant.

CHAPTER 2

RADIATIVE HEAT TRANSFER ANALYSIS

2.1 Background

Solid oxide fuel cells (SOFCs) operate at temperatures on the order of 600-1000 ^{o}C [6]; thus, radiation heat transfer must be given special consideration in thermal modeling efforts, including stack thermal management and materials development. During the last decades, a number of increasingly detailed theoretical and numerical models of the coupled electro-chemical, thermal, and fluid processes in SOFCs have been developed, and multiple papers have been published on the subject. The first modeling efforts were highly simplified and limited to predicting average cell values such as voltage, current density and temperature in isothermal cells—which sidesteps the issue of thermal radiation altogether. More detailed, non-isothermal numerical models (for example [7-9]) began to appear in the early 1990's, and building on these pioneering works, Hartvigsen, et al.[10] were the first to consider surface-to-surface radiation exchange in thermal models of SOFCs and concluded that it was significant. Since that time, many papers have reported results of numerical calculations, some including the effects of radiation (for example, see references [11-16]), and others not. The methodologies employed vary from highly simplified analysis to much more detailed, computationally expensive methods (often via commercial CFD codes) with sometimes conflicting results and conclusions reported.

The goal here is to establish a complete picture of how radiation heat transfer should be treated in different components of SOFCs and identify and properly validate the justifiable simplifying assumptions that ease the computational burden without compromising the

validity of the analysis. First, radiative heat transfer in the semitransparent anode (positive electrode)-electrolyte-(negative electrode) cathode, or simply PEN structure of the SOFC unit cell, is considered and its effect on the overall operating conditions is evaluated. Next, the discussion is extended to modeling surface-to-surface radiation exchange in the flow (air and fuel supply) channels, including the effects of participating gases in the channels. Finally, stack level thermal radiation effects including recent developments [17, 18] in the area of high temperature thermal insulation and overall stack thermal management are analyzed and future research areas identified.

From a heat transfer perspective, the unit cell operates as a heat exchanger, dissipating heat generated by the irreversible electrochemical conversion of fuel (hydrogen or reformate in the case of SOFC with internal hydrocarbon fuel reformation) to electricity. On the cathode side, oxygen molecules diffuse through the porous electrode and are reduced at the interface of the cathode and electrolyte. These ions travel through the electrolyte and combine with dissociated hydrogen (at the electrolyte-anode interface), which has diffused through the anode from the fuel channel [6] (see Figure 1). The irreversibilities of electrochemical reactions and the electrical resistance to flow of ions through the electrolyte generate heat, which is carried out of the cell by the flowing gases in the channels. The heat transfer from this region of generation to the ultimate heat sink (ambient) involves radiative transfer in participating media such as electrodes, electrolyte, and participating gases in the channels, as well as surface-to-surface radiation exchange in the channels.

On the other hand, in a stack of many unit cells, it is desirable to maintain uniform temperature profiles and not allow cells near the edges to operate at lower temperatures than cells in the interior of the stack. Thus, management of heat losses from the stack, through the

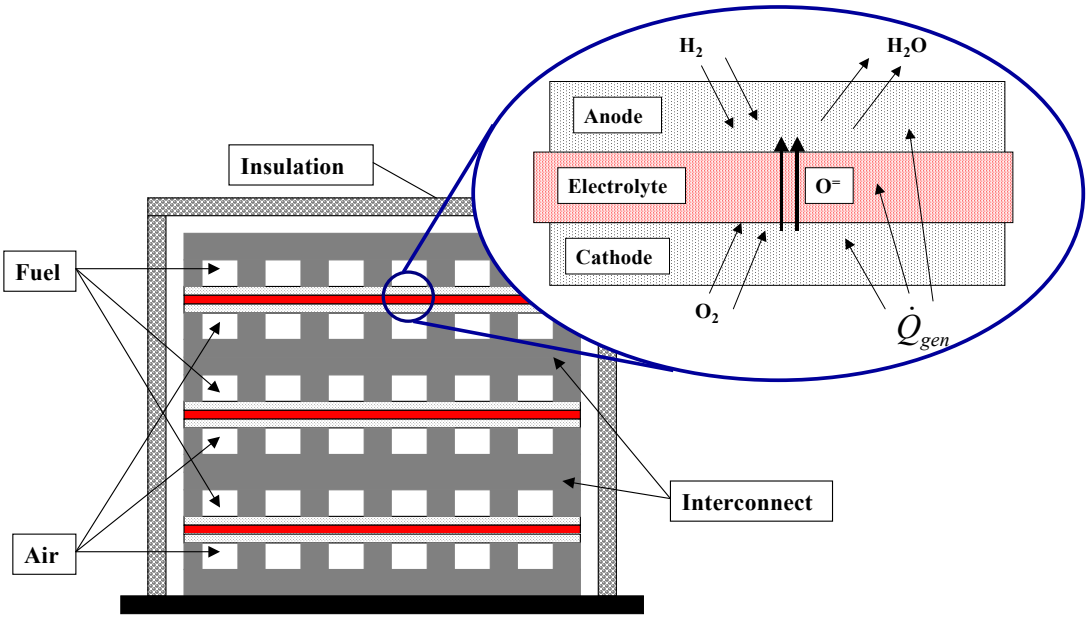

Figure 1. Schematic of a planar SOFC stack consisting of numerous individual unit cells. Radiation effects are important on various levels: (1) within each individual cell, (2) between the cell stack and insulation, (3) within the insulation, and (4) between the insulation and surroundings.

insulation, to the environment is of critical importance in maintaining the overall efficiency of the stack, and prohibiting the development of damaging thermal gradients. The design of high temperature thermal insulation involves an analysis of radiative transfer in participating media (within the insulation materials), while the transfer of heat from the stack to the insulation and to the environment can be modeled as surface-to-surface radiation exchange.

Inclusion of radiative transfer in analysis of heat transfer entails a number of challenges which are particular to thermal radiation modeling and not encountered in analysis of convective-conductive heat transfer. The first is the inherent complexity of the governing equations which are integro-differential and, in general, depend on as many as seven independent variables (time, three position variables, two angular variables describing direction of propagation of radiation rays, and the wavelength). Further, the governing equations are non-linear, as the emissive power features a fourth-power dependence on

temperature. Besides the difficulty associated with solving these equations, the accuracy of any analysis is always limited by the extent to which radiative properties are known. Unlike the thermophysical properties relevant to conduction or convection heat transfer, which are well behaved, rather well characterized, and usually weakly dependent on temperature, radiative properties are often highly (even erratically) dependent on wavelength of radiation and surface preparation, and a strong function of the temperature. Furthermore, in many cases limited experimental data exists for radiative properties, and even that is for the materials relevant to power generation and aerospace applications. Fortunately, in certain cases making use of carefully justified simplifying assumptions renders these difficulties manageable and allows one to obtain results sufficiently accurate for engineering calculations. Even a simplified analysis can be very costly, however, increasing computational time requirements by an order of magnitude or more [11, 15] as compared to the conductive-convective heat transfer calculations alone. This fact motivates us not only to discuss the existing modeling methodologies and simplifying assumptions for treating radiative heat transfer, but also to specify the conditions under which certain radiative effects could be neglected altogether.

2.2 Radiative transfer in participating media

In a previous work [11] a framework for modeling radiation within the optically thick porous electrodes, and optically thin yttria-stabilized zirconia (YSZ) electrolyte, was developed. It was shown that the radiative effects are significant for thicker, semitransparent electrolytes, reducing the overall operating temperature (by 150 K) and decreasing thermal gradients in the monolith type cell. Also, it was shown that the Schuster-Schwarzchild's two-flux approximation gives accurate results at a fraction of the computational cost of the

discrete ordinates (DO) method. In that work, however, knowledge of the relevant radiative properties was limited, and the models were developed assuming gray properties.

Here, experimental measurement of optical properties of the SOFC materials is reported. Since the optical properties exhibit significant spectral variation, the radiative transfer model is formulated on a spectral basis, still in the optically thin limit of the two-flux approximation, and used to solve the radiative transfer equation (RTE) in the YSZ electrolyte layer. The divergence of the total radiative heat flux is then incorporated into the overall energy conservation equation as a heat sink term through the user defined function utility in the FLUENT CFD model of the SOFC. The cell geometry under consideration is shown in Figure 2, with relevant dimensions, properties, and operating conditions given in Table 1.

2.2.1 Measurement of radiative properties

In general, the electrolyte and the porous electrodes of SOFCs are semitransparent materials; that is they can absorb, scatter, and emit thermal radiation. For a linear medium, the spectral absorption coefficient, κ, refractive index, *n,* spectral scattering coefficient, σ_s,

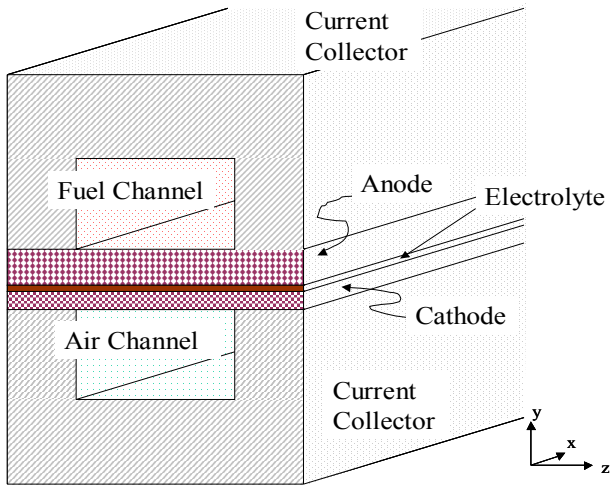

Figure 2. Schematic of the planar, anode-supported unit cell model of SOFC (not to scale).

Table 1. SOFC Unit Cell Dimensions, Material Properties, and Operating Conditions

Region	Type	Size/Thickness	Density [kg/ m^3]	Thermal Conductivity [W/m K]
Cathode	Porous (0.3)	75 μm	3030	5.84
Anode	Porous (0.4)	500 μm	3310	1.86
Electrolyte	Solid	15 μm	5160	2.16
Current collector	Solid	5 mm	8030	20.0
Cell Length (x-direction)		10 cm		
Cell Width (z-direction)		5 mm		
Air/Fuel Channels		2.5 x 3.0 mm		
Fuel Inlet (1000 K)	80% H_2	20% H_2O		85% utilization
Air Inlet (1000 K)	21% O_2	79% N_2		20% utilization

and the scattering phase function, Φ, provide a complete set of phenomenological properties required to model the propagation of radiative energy in the medium. In addition, emissivity, ε, and reflectivity, ρ, of the bounding interfaces must be provided in order to specify the boundary conditions. These radiative properties typically vary with wavelength, and we used Planck's law [19] to find the relevant spectral range for measurements. For typical operating temperatures of 900-1100 K and refractive index of the electrolyte, $n \approx 1.8$ [11], it can be shown that over 90% of the emissive power is contained within the near to mid infrared spectral region, $0.9 < \lambda < 7.8\ \mu m$. Figure 3 shows the emissive power as a function of wavelength for these conditions.

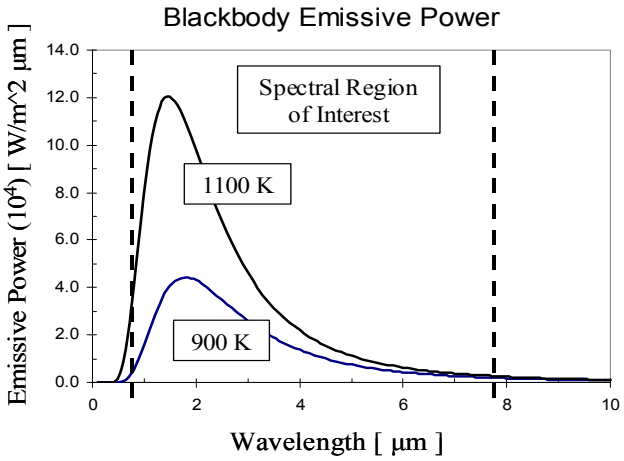

Figure 3. Definition of the spectral range of interest wherein 90% of radiative energy falls according to Planck's law for blackbody emissive power (n =1.8) for the temperatures relevant to SOFCs.

A Fourier transform infrared (FTIR) spectrometer (Bruker Optics TENSOR 37) fitted with a reflectance accessory was used to obtain transmittance, *Tr*, and reflectance, *R*, data for samples of YSZ, nickel-doped YSZ, and strontium-doped Lanthanum ferrite (LSF)—materials commonly used for the electrolyte, anode, and cathode, respectively, of SOFCs. For collecting near-IR data, an InGaAs detector and quartz beam splitter were used, and for the mid-IR data, a KBr/DLaTGS collector and Ge on KBr substrate beam splitter were used. All measurements were performed at room temperature. For 200 μm thick samples of Ni-YSZ, and LSF, the transmittance was essentially zero within the noise of the measurements. Thus, it is assumed that the electrodes are opaque in this region of the spectrum, although scattering could play a role in radiative transfer and should be investigated further. The 330 μm thick sample of polycrystalline YSZ, however, is semitransparent and shows significant spectral variation in transmittance and reflectance as seen in Figure 4.

This transmittance and reflectance data can be related to the transmittivity, τ, and reflectivity, ρ, through geometric optics and ray tracing methods [19] via simultaneous solution of the following equations:

$$R = \rho\left[1 + \frac{(1-\rho)^2\tau^2}{1-\rho^2\tau^2}\right] \tag{1}$$

and,

$$Tr = \frac{(1-\rho)^2\tau}{1-\rho^2\tau^2} \tag{2}$$

Once transmittivity and reflectivity are calculated, the absorptive index, k, is found from,

$$k = -\frac{n\lambda\ln[\tau]}{4\pi d} \tag{3}$$

where, d is the thickness of the sample. The refractive index, n, can be approximately found

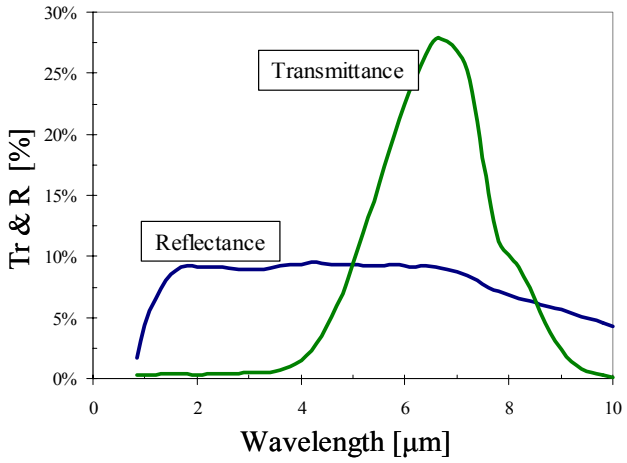

Figure 4. FTIR transmittance and reflectance data for a 330 μm thick sample of polycrystalline yttria-stabilized zirconia (YSZ).

using Fresnel's equation [19] by assuming that the material of interest has low absorptive index, and for near normal incidence,

$$\rho = \frac{(1-n)^2 + k^2}{(1+n)^2 + k^2} \tag{4}$$

Finally, the spectral absorption coefficient, κ, is related to the absorptive index by,

$$\kappa = \frac{4\pi k}{n\lambda} \tag{5}$$

where, λ is the wavelength of the radiation. The resulting absorption coefficient, found by processing FTIR data using the method described above, is given in Table 2 and plotted in Figure 5. For a typical electrolyte thickness of 15 μm, the resulting spectral optical thickness, τ_λ, of the electrolyte layer varies between 0.07 and 0.24 in the spectral region of interest. Thus, a spectral, optically thin approximation is appropriate for solving the radiative transfer equation in the electrolyte [19].

Table 2. Absorption Coefficient and Refractive Index of YSZ

Wavelength, λ [μm]	Absorption Coefficient, κ [cm^-1]	Refractive Index
1.0	172	1.38
1.5	165	1.79
2.0	163	1.90
2.5	162	1.80
3.0	159	1.83
3.5	148	1.86
4.0	121	1.88
4.5	90	1.88
5.0	66	1.87
5.5	50	1.85
6.0	40	1.84
6.5	34	1.82
7.0	35	1.79
7.5	47	1.75
8.0	65	1.71
8.5	79	1.67
9.0	109	1.63
9.5	152	1.58
10.0	203	1.52

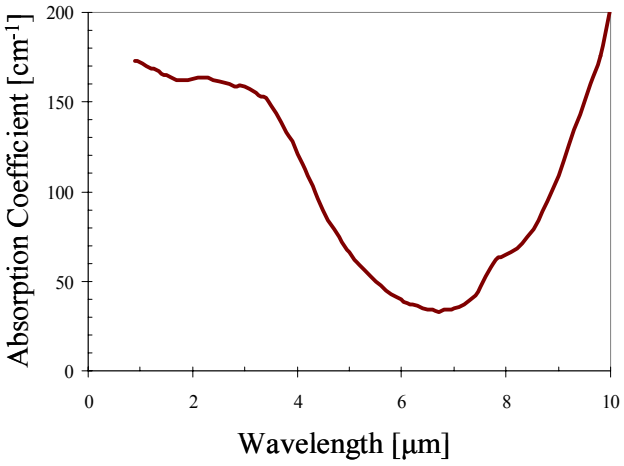

Figure 5. Absorption coefficient of YSZ computed from transmittance and reflectance measurements showing strong spectral dependence.

2.2.2 Formulation of radiative transfer model

Modeling of thermal radiation propagation in participating media requires solution of the radiative transfer equation (RTE), an integro-differential equation which cannot be solved analytically in its most complete form [19]. It is convenient to write an RTE in terms of the

spectral optical thickness, $\tau_\lambda = \int_0^s \beta_\lambda ds$, which is a rescaled spatial variable, *s,* in the direction of radiation beam propagation with the spectral extinction coefficient, $\beta_\lambda = \kappa_\lambda + \sigma_\lambda$, acting as scaling factor. In quasi-steady state form, with the given change of variables, the RTE is,

$$\frac{dI_\lambda}{d\tau_\lambda} = -I_\lambda + (1-\omega_\lambda) I_{b\lambda} + \frac{\omega_\lambda}{4\pi} \int_{4\pi} I(\hat{\mathbf{s}}_i) \Phi(\hat{\mathbf{s}}_i, \hat{\mathbf{s}}) d\Omega_i \tag{6}$$

where I_λ is the spectral intensity of radiation, $I_{b\lambda}$ is the blackbody intensity of radiation (function of the local temperature), $\omega_\lambda = \sigma_\lambda / \beta_\lambda$ is the single scattering albedo (ratio of radiation decay by scattering to the total extinction of radiation), and $\Phi(\hat{s}_i, \hat{s})$ is the scattering phase function, which upon integration over the entire hemisphere in Eq. (6) gives augmentation of radiation via in-scattering (i.e., redirection of radiation from other directions to the given direction). The radiative heat flux at any point within the medium can be computed from the spectral intensity of radiation (after it is determined by solving Eq. (6)) by integration over all possible directions of radiation propagation as well as over the entire electromagnetic spectrum,

$$q_r = \int_0^\infty \int_{4\pi} I_\lambda(\hat{\mathbf{s}}) \hat{\mathbf{s}} \, d\Omega d\lambda \tag{7}$$

Solving Eq. (6) in the most general case of a three-dimensional, spectrally-dependent, absorbing-scattering-emit-ting medium is a formidable task even when it is done numerically. Therefore, it is beneficial to employ several simplifying assumptions that allow approximate solution of the problem.

First of all, the typical SOFC unit cell geometry features very thin (high aspect ratio) layers of electrode and electrolyte materials arranged in either plane-parallel (planar design)

or cylindrical/concentric (tubular design) fashion, thereby making a one-dimensional heat transfer approximation well justified. This reduction in dimensionality of the problem reduces the complexity significantly. Second, the experimental data suggest that SOFC electrodes are opaque and, therefore, volumetric radiation can be neglected or treated in the limit of the optically thick media approximation, for which the optical distance, $\tau_L = \beta L \gg 1$, if the extinction coefficient is known. In this case, the very simple, Rosseland approximation [19] can be invoked since the mean free path for photon propagation is short and radiation propagation can be treated as a diffusion process. On the other hand, the YSZ electrolyte appears to be optically thin ($\tau_L \leq 1$), and in the case of a 1-D, plane parallel medium the Schuster-Schwartzchild two-flux approximation can be used to reduce the RTE to a second-order ODE for spectral radiative heat flux.

The Schuster and Schwartzschild's, or two-flux, approximation assumes that the radiative intensity is uniform over the upper and lower hemispheres. Also, assuming isotropic scattering in the YSZ, the RTE can be rewritten as an ODE for the spectral heat flux

$$\frac{d^2 q_\lambda}{d\tau_\lambda^2} - (1-\omega_\lambda)(4q_\lambda) \quad = \quad (1-\omega_\lambda)4\frac{dE_{b\lambda}}{d\tau_\lambda} \tag{8}$$

where, q_λ is the spectral radiative heat flux, and $E_{b\lambda}$ is the spectral, black-body emissive power. The boundary conditions for diffuse surfaces can be expressed, after some manipulation, as,

$$\begin{aligned} \tau_\lambda = 0: \quad & -\frac{(1-\rho_1)}{1-\omega}\frac{dq_\lambda}{d\tau_\lambda} + 2(1+\rho_1)q_\lambda = 4(\varepsilon E_{b\lambda})_1 - (1-\rho_1)4E_{b\lambda} \\ \tau_\lambda = \tau_{\lambda,L}: \quad & -\frac{(1-\rho_2)}{1-\omega}\frac{dq_\lambda}{d\tau_\lambda} - 2(1-\rho_2)q_\lambda = 4(\varepsilon E_{b\lambda})_2 - (1-\rho_2)4E_{b\lambda} \end{aligned} \tag{9}$$

where, ρ is the reflectivity of the boundaries, (subscripts 1 and 2 indicate properties at the boundaries), ε is the emissivity of the boundaries, and $\tau_{\lambda,L}$ is the spectral optical thickness of the 1-D layer. Equation (8) was solved for spectral radiative heat flux as a function of spectral optical thickness, however, the solution obtained is only semi-analytical, containing integrals of the blackbody emissive power that were numerically approximated. (See Appendix A for the complete solution.)

Once the spectral radiative heat flux is determined, total radiative heat flux is obtained by integration of the spectral heat flux over the entire electromagnetic spectrum,

$$q_r = \int_0^\infty q_\lambda d\lambda \tag{10}$$

Numerically, the spectral integration is accomplished through the N-band approximation method [19, 20], which assumes that spectral properties, (in this case the extinction coefficient), are approximately constant over discrete wavelength intervals and replaces the integral by a summation.

2.2.3 Model validation

In order to validate the semi-analytical solution for solving the spectral RTE for the optically-thin electrolyte, the numerical solution was compared to an analytical solution given by Modest [19] for an isothermal problem as well as to a simple 1-D combined conduction-radiation problem solved using FLUENT's built in Discrete Ordinates (DO) method.

The radiative heat flux in a gray, isothermal, non-scattering, 1-D, plane-parallel medium between two black walls at equal temperatures (Figure 6), is given analytically by

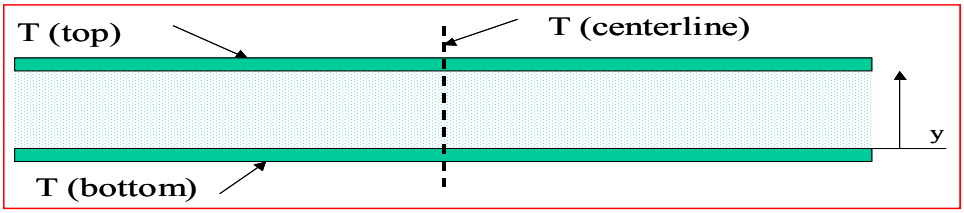

Figure 6. A simple problem of radiation-conduction heat transfer in a 1-D, plane-parallel medium bounded between two isothermal plates used for validation of the spectral two-flux radiation model.

the following two-flux approximation [15],

$$q = n^2\sigma(T^4 - T_w^4)\left[e^{-2(\tau_L-\tau)} - e^{-2\tau}\right] \tag{11}$$

where, σ is the Stefan-Boltzmann constant, T and T_w are the absolute temperatures of the medium and walls, respectively, and τ is the optical length. A dimensionless heat flux is then defined as:

$$\Psi = \frac{q}{n^2\sigma(T^4 - T_w^4)} = e^{-2(\tau_L-\tau)} - e^{-2\tau} \tag{12}$$

Figure 7 compares numerical predictions of the wall heat flux obtained using the spectral algorithm (with gray properties) and the analytical solution given by Eq. (12). In the simulations, the temperatures of the walls and medium are taken to be 1000 *K* and 900 *K*, respectively. Clearly, the results agree very well for optical thickness up to approximately 2.0.

Further validation of the solution algorithm demands comparison of the results for the problem involving both radiation and conduction. To this end, the spectral two-flux model was implemented in FLUENT CFD software as a user defined function (UDF), which incorporates the divergence of the radiative heat flux as a heat sink in the energy equation. In order to validate this implementation, a simple problem was considered of combined radiative-conductive heat transfer in a 1-D, plane-parallel medium bounded by two

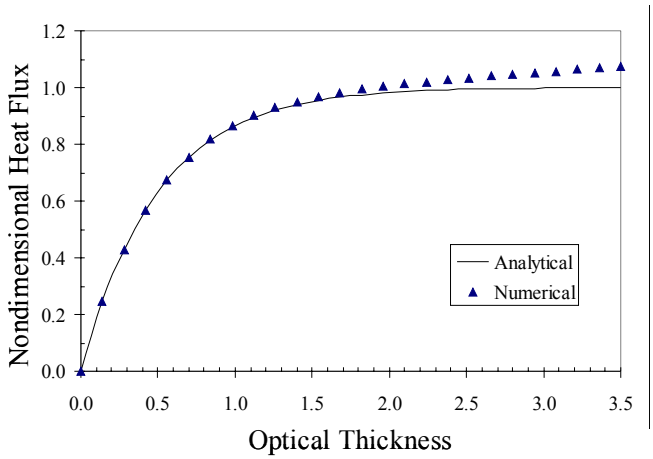

Figure 7. Comparison of the numerical predictions obtained using the spectral two-flux model with the analytical solution (eqn.(12)) for the non-dimensional wall heat flux.

isothermal plates (Figure 6). The temperatures of the upper plate and lower plate were fixed at 1200 *K* and 800 *K*, respectively. The temperature field within the medium was solved using the discrete ordinate (DO) method (standard FLUENT implementation) as well as by using the UDF for the two-flux approximation that was developed. A comparison of the results for optical thickness of 0.001, 0.1, and 1.0 shown in Figure 8 clearly indicates the robustness of the developed spectral two-flux radiation-modeling algorithm.

In addition to testing the two-flux model implementation on these gray problems, a spectral case was also considered by using three spectral bands to approximate the spectral dependence of the extinction (absorption) coefficient of the electrolyte (obtained from measurement results in Table 2),

$$\beta = \begin{Bmatrix} 160\ cm^{-1}; & 0.0 < \lambda < 3.5 \\ 110\ cm^{-1}; & 3.5 \le \lambda < 5.0 \\ 50\ cm^{-1}; & 5.0 \le \lambda < \infty \end{Bmatrix} \tag{13}$$

These values correspond to optical thicknesses of 0.24, 0.165, and 0.075 for three respective spectral bands in the case of a 15 μm thick electrolyte. Figure 8 shows a comparison between

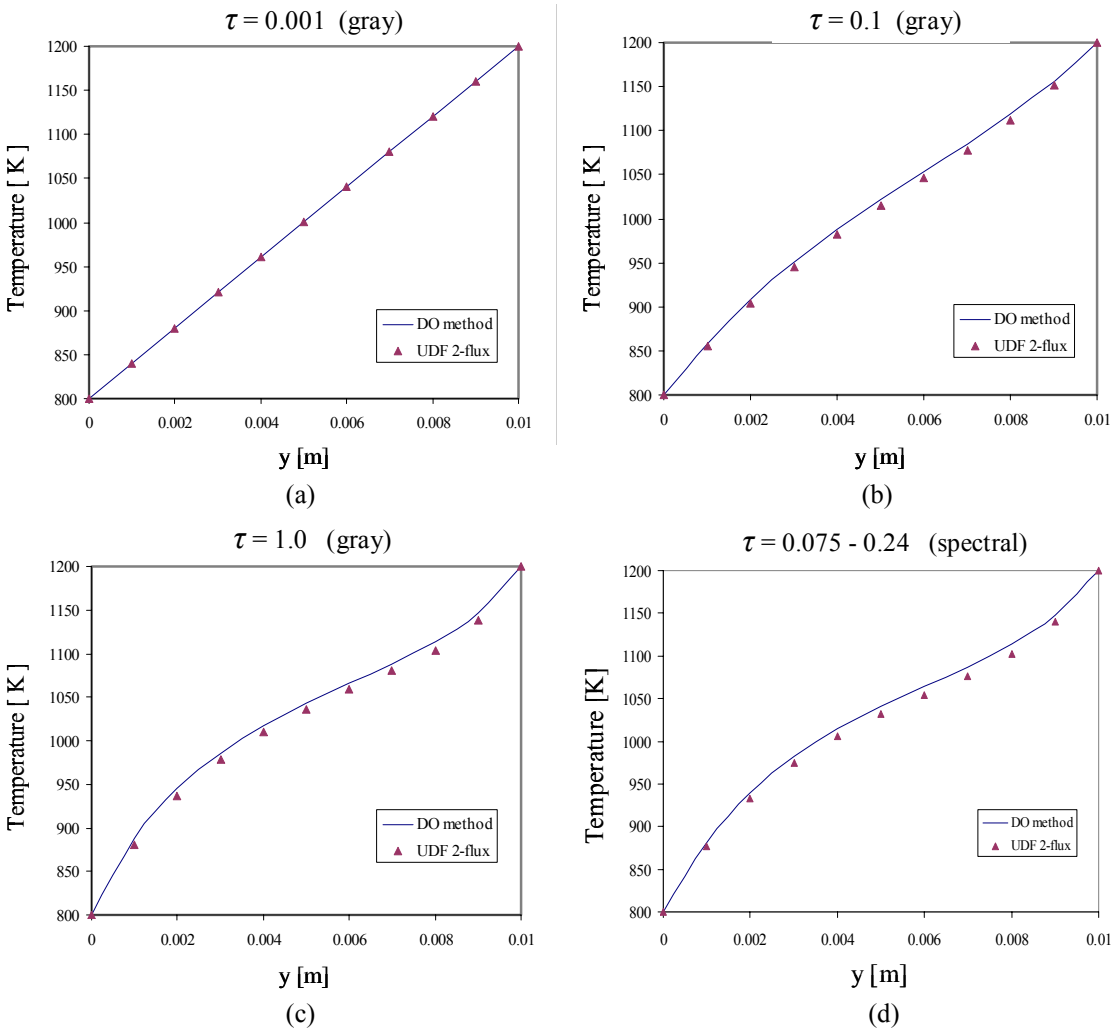

Figure 8. Comparison of results obtained using the two-flux and discrete ordinates (DO, benchmark) methods for various optical thicknesses and gray optical properties (a-c), and spectrally varying absorption coefficient (d).

the temperature predictions obtained using the two-flux model and FLUENT's standard discrete ordinate method for the 3-band spectral model. In this simulation, the boundaries were assumed gray (ε = 0.9), with an isotropically scattering medium (ω = 0.l). Once again, the agreement appears to be satisfactory. Although the medium is assumed to be isotropically scattering, the single scattering albedo is not known, and for the remainder of this analysis, was assumed zero.

2.2.4 Model Results and Analysis

Solution of the momentum, energy, and species conservation equations that describe species transport and the temperature field in the unit cell of an SOFC stack was obtained using FLUENT CFD software as described in the previous work [11]. The electrochemical reactions and the potential field within the cell were solved by an add-on tool developed by the Department of Energy's National Energy Technology Laboratory, which is described in the literature [21, 22]. The unit cell geometry, material properties, and the standard operating conditions under consideration are given in Table 1. The FLUENT model of the SOFC unit cell was discretized using a fine mesh of 105,600 elements. The appropriateness of this mesh was verified against another model of 262,500 elements, and the results from both compared favorably. Because the unit cell is part of a larger stack, the boundaries were treated as adiabatic. The electrodes were modeled as porous media, and the electrolyte as a solid region. In this model, the current density of the cell was specified (150 mA/cm^2), resulting in an average operating voltage of 0.87 V and average cell temperature of 1046 K.

Because the temperature gradients at interfaces are of particular interest for thermo-mechanical failure analysis, Figure 9 shows a comparison of the temperature distribution at the anode-electrolyte and cathode-electrolyte interfaces for the cases with and without radiation in the electrolyte layer. Clearly, the effect of radiation is minimal, leading to at most a couple of degrees reduction in the interfacial temperature. This is in sharp contrast to the previous findings [11], wherein significant reduction in temperature was reported when radiation is included. This significant difference in results owes to difference in 1) radiative properties of YSZ and 2) cell geometry that was simulated in [6] and here. Specifically, the absorption coefficient for *polycrystalline* YSZ experimentally measured and reported here is

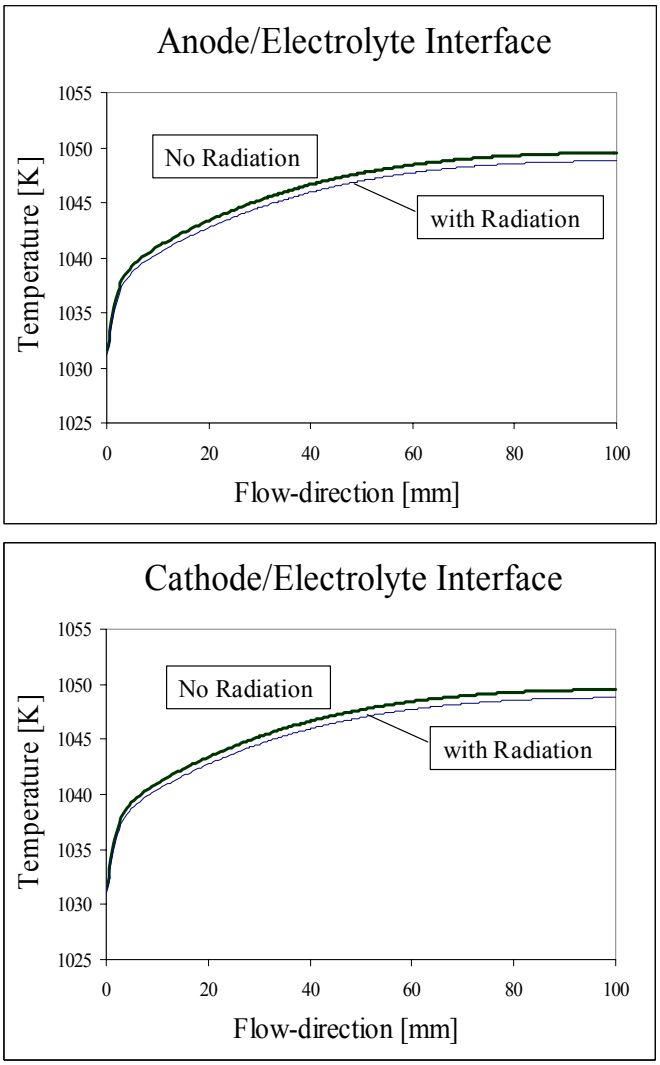

Figure 9. Temperature profile of the anode/electrolyte and cathode/electrolyte interfaces with and without radiation.

at least an order of magnitude greater than that of *single crystal* YSZ used in [11]. Also, in the previous work a thick, 500 μm electrolyte layer was used, leading to significant (relative to thermal radiation) conduction resistance. With the correct properties of YSZ now available, the optical thickness of the 500 μm electrolyte ranges from 2 – 7 (optically thick) vs. 0.25 previously calculated in [11]. This has the effect of greatly reducing radiative transfer due to the exponential decrease in transmittance that occurs with an increase in optical thickness. In the current case of a more realistic electrolyte thickness (15 μm or less)

found in state-of-the-art SOFCs [22-24], the conduction resistance across the electrolyte is reduced by a factor of more than 30. Combined with the increase in radiation resistance just mentioned, the net result is dominance of conduction heat transfer over radiative heat transfer even for such high operating temperatures as found in SOFCs. Thus, the disparity in results from the previous work vs. the current work is fully explained from a physical standpoint.

In SOFCs, heat generated by the electrochemical reactions at the electrode-electrolyte interfaces and by ohmic heating in the electrolyte is carried away mostly by flow in the air channel. Thus, the electrolyte acts as a thermal resistance to removing heat generated at the interface of the anode and electrolyte. It can be shown that for the geometry and operating conditions reported in [11], radiative heat transfer contributes approximately 15% to the total heat flux across the electrolyte in the presence of only 1 K temperature difference across the electrolyte at temperatures relevant to SOFCs. This is not the case when the corrected radiative properties are used, or for a very thin electrolyte, which must sustain much greater temperature gradients before radiation becomes significant.

Finally, although our results indicate that radiation within the electrolyte has little effect for the geometry and operating conditions used in this study, it cannot, in general, simply be neglected. For example, during the start-up and shut-down of the SOFC, one could develop significant temperature gradients across even very thin electrolyte leading to potentially significant radiation effects. The major concern on whether or not to include the radiation analysis into the SOFC thermal model lies in the tremendous increase in computational costs associated with inclusion of radiation. This demands development of computationally efficient techniques for treatment of radiative heat transfer.

The spectral two-flux model developed here is sufficiently accurate and adds only 20% to the CPU time required to obtain the converged solution of the overall SOFC thermal-fluid model. This is in comparison to the approximately ten-fold increase in the CPU time required for computations if radiation is solved using the standard discrete ordinate (DO) method implemented in FLUENT. Thus, we would argue that the spectral two-flux treatment of radiative heat transfer is sufficiently accurate and computationally efficient to be included in any SOFC thermal-fluid analysis tool to study, on a case-by-case basis, variations in geometry, operating conditions, or electrolyte materials that could potentially induce significant temperature gradients across the electrolyte layer.

2.3 Surface radiation in flow channels

In this section, we consider radiative transfer in the flow channels which are used to supply the fuel (hydrogen or hydrocarbons) and oxidizer (air) to the cell PEN structure and are bounded by hot (emitting radiation) walls. In general, one needs to consider emission and reflection of radiation by the walls as well as its extinction (absorption and scattering) and emission by the flowing gases.

2.3.1 Radiative properties

Air mainly consists of simple non-polar nitrogen and oxygen molecules and, therefore, is non-interacting (transparent) with thermal radiation at the moderate pressures and temperatures found in SOFCs [19]. Therefore, no bulk extinction and emission of radiation takes place, limiting the radiative transfer to surface-to-surface exchange of radiative energy. For the fuel channels, however, the analysis is more complicated due to the presence of the following participating species: H_2O, CO_2, CO, CH_4, and possibly other hydrocarbons. Radiative properties of these gases are well established (at high temperatures)

and show very strong spectral, temperature, and pressure dependence [19]. Therefore, an accurate treatment of spectral emission and absorption by gases can quickly become very involved with more than a half of a dozen of advanced, competing models available, each of them still with somewhat limited range of validity.

Here, we are more interested in a simplified analysis in order to establish whether or not radiation transfer in gases should be considered at all or if gases can be treated as essentially non-participating medium as far as SOFC fuel flow channels are concerned. To this end, the concept of the *Planck-mean absorption coefficient* becomes very useful for this approximate analysis. From the literature data (see, for example, Modest [19]) these spectrally-averaged absorption coefficients are approximately: 0.1 $cm^{-1}bar^{-1}$ for H_2O; 0.3 $cm^{-1}bar^{-1}$ for CO_2 and CO; and 0.4 $cm^{-1}bar^{-1}$ for CH_4 at 600 ºC. A quick calculation of the optical thickness of the fuel channel across its diameter (~5 *mm*) for a typical fuel stream composition yields $\tau_L < 0.1$ at atmospheric pressure, leading to gas transmittance, $Tr = \exp\left[-\tau_L\right]$, approaching unity—implying that the medium can be treated as transparent. Surface-to-surface radiation exchange is thus the only radiative transfer mode that must be considered in the flow channels of SOFC unit cells. From the property perspective, the only required input to this model is the emissivity of the relevant materials, which is not well known and can vary significantly depending on temperature and redox state. Finally, it should be noted that this conclusion is strictly valid for the air/fuel supply channels with very high aspect ratio only.

2.3.2 Model formulation

Here, we review the net radiosity method [19] for calculating the radiative heat flux between surfaces in a channel (planar and tubular cell) separated by a transparent medium,

and comment on some simplifications that can be made to the analysis under certain conditions. As a first approximation, one can assume that the walls are opaque, gray, diffuse emitters and reflectors of thermal radiation, especially in the absence of more detailed property data. However, in the case when one of the walls is a porous surface of the electrode, this assumption may be questionable and the analysis becomes proportionately more complex. One way to avoid this difficulty is to assign an apparent emissivity and reflectivity to the porous electrode interface, which can be computed or measured by considering the entire porous electrode layer. By forming an enclosure based on the flow channel geometry (where all openings are closed by virtual black surfaces maintained at 0 *K*), the radiative heat flux at any point on the surface of the flow channel is given by

$$\frac{q(\mathbf{r})}{\in(\mathbf{r})} - \int_A \left(\frac{1}{\in(\mathbf{r}')} - 1 \right) q(\mathbf{r}')\, dF_{dA-dA'} + H_o(\mathbf{r}) = E_b(\mathbf{r}) - \int_A E_b(\mathbf{r}')\, dF_{dA-dA'} \qquad (14)$$

where, $dF_{dA\text{-}dA'}$ is the diffuse shape (view) factor between two surface elements dA and dA', ε is the emissivity of the surface, $E_b = \sigma T^4$ is the black-body emissive power, and H_o is incident radiation entering or leaving the enclosure through a virtual surface (can be used to couple analysis of the flow channel with radiation to/from the cell surrounding/manifolds). Notice that in order to solve Eq. (14) for heat flux, the temperature at every point in the enclosure must be known as well as the emissivity. However, the flow channels in the planar-type fuel cells typically have high aspect ratio (L/d ~30), and, therefore, following the conclusions reached in papers [25-27], the walls can be treated as black surfaces with emissivity equal to 1. This greatly simplifies the analysis and the radiative heat flux at any point on the channel walls can be expressed as,

$$q_r = E_b(\mathbf{r}) - \int_A E_b(\mathbf{r}')\, dF_{dA-dA'} - H_o(\mathbf{r}) \qquad (15)$$

The view factor $dF_{dA\text{-}dA'}$ in Eqs. (14) and (15) physically represents the fraction of radiation leaving surface element *dA* that is incident on another surface element *dA'* without any intermediate reflections, i.e., via direct travel (see Figure 10). View factors are geometric quantities which can be evaluated analytically, numerically, or by consulting tabulated values [19]. The view factors between elements on the channel walls and inlet/outlet elements diminish to zero very rapidly with distance from the end [26]. The view factors between elements at fixed axial positions (i.e., on top of each other) are relatively large, but the temperature differences between the wall surface elements at a given axial position are relatively small in a typical fuel cell. Thus, radiative heat flux is not expected to have a large effect on the average operating temperature of the cell, although some have indicated as much as a 30 *°C* decrease in maximum temperature and a flattening of the temperature profile with the inclusion of surface radiation in planar cell channels [12, 15].

It is important to point out the fundamental difference between a tubular cell channel and planar cells in analyzing the flow channel radiation exchange. In the tubular cell, radiation exchange is between the surfaces of two concentric tubes, the air supply tube and the porous support tube (Figure 11), and the black surface approximation would not generally be appropriate. However, there does exist symmetry in the radial direction that allows the channel to be discretized into *N* isothermal slices unlike the channels in planar cells. Figure 12 shows this schematically, and gives an indication of the view factors that should be

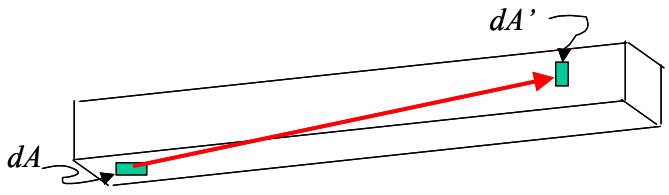

Figure 10. Schematic to aid in view factor definition for two surface elements in a planar cell flow channel.

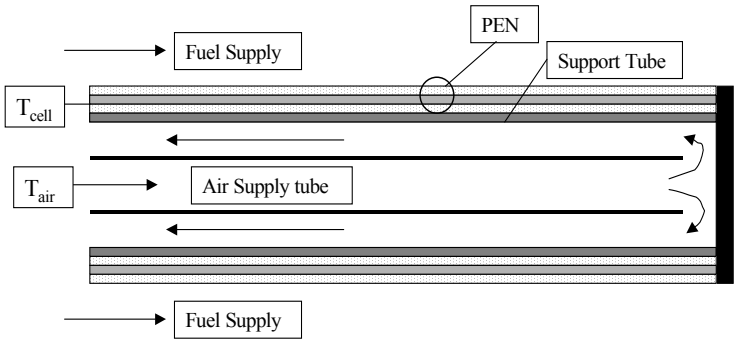

Figure 11. In a tubular cell [9,10], thermal radiation from the outer supporting air tube to the air supply pipe is the dominant heat transfer mechanism due to the large temperature difference between the two surfaces.

be appropriate. However, there does exist symmetry in the radial direction that allows the channel to be discretized into *N* isothermal slices unlike the channels in planar cells. Figure 12 shows this schematically, and gives an indication of the view factors that should be calculated. Depending on geometry of the channel, some of these view factors may be negligible or vanish quickly in the axial direction. Once again, this must be determined on a case-by-case basis.

2.3.3 Coupling of radiation to energy equation

Once radiative heat flux at the surface is calculated, it can be incorporated into overall energy conservation through the boundary conditions at the walls,

$$q_{\mathbf{conv}} + q_{\mathbf{rad}} = q_{\mathbf{cond}} \rightarrow h\left(T_b - T_\infty\right) + q_{\mathbf{rad}} = -k\left.\frac{\partial T}{\partial n}\right|_{boundary} \tag{16}$$

Comparison of the magnitude of the convective and radiative heat fluxes will give an indication of which heat transfer mode is dominant, and which, if any, can be neglected.

2.4 Stack level thermal radiation

Here we review several topics related to thermal radiation from a stack of unit cells to the environment. In particular, recent work on high temperature insulation systems for

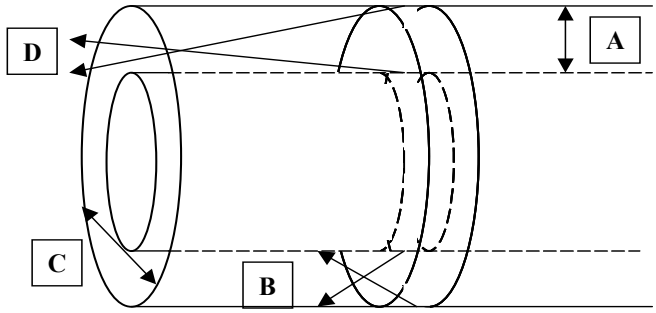

Figure 12. View factor calculation for the isothermal slices on two concentric tubes: (A) the inner surface "sees" the outer surface of the same slice and vice versa, (B) both surfaces see other slices along the axial direction, (C) the outer surface sees itself, (D) both surfaces of a given slice see the external environment.

SOFC application completed by Spinnler, et al. [17, 18], is an excellent example of the approach that should be followed in future work. Also, we provide guidelines and a framework for future work in stack thermal management, including identification of objectives and methodology for proper accounting of thermal radiation effects.

2.4.1 Radiative properties

Recently, Spinnler, et al. [17, 18], published an excellent theoretical and experimental analysis of high temperature insulation for application to SOFC stacks. The insulation design considered by these authors featured multi-layer thermal insulations (MTIs), wherein highly reflective screens are separated by insulating, opaque spacers as shown in Figure 13. The screens increase the overall thermal resistance of the MTI by reflecting thermal radiation back towards the hot side. Several screen materials such as gold, ceramic, and stainless steel have been considered with reflectivity ranging from high to low values, respectively. The spacer materials considered by the authors were of the fibrous (thermal conductivity, $k \sim 0.1$-$0.35\ W\ m^{-1}K^{-1}$) and microporous ($k \sim 0.02$-$0.04\ W\ m^{-1}K^{-1}$) type with known absorption and scattering characteristics. The goal of the analysis was to develop a thermal model for MTIs that predicts the experimentally measured effective thermal conductivity, given material selection and configuration.

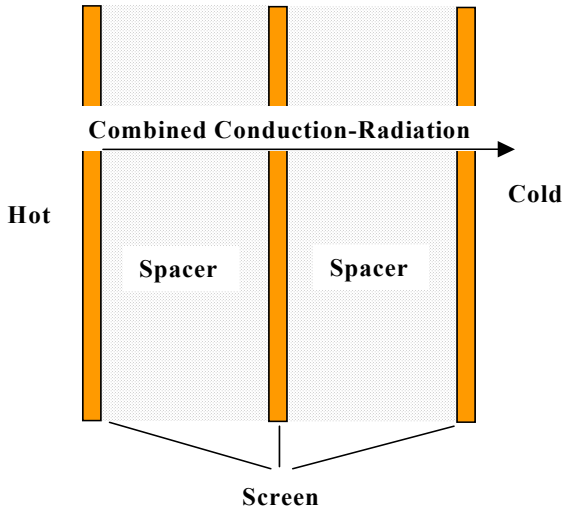

Figure 13. Multilayer thermal insulation (MTI) wherein opaque, insulating spacer materials are separated by reflective screens which reduce the heat loss by back-reflecting thermal radiation [17,18].

2.4.2 Radiation model

The analysis was done in the limit of steady, one-dimensional conductive-radiative heat transfer in the plane-parallel layer of insulation. It was determined that the Rosseland diffusion approximation underestimates the influence of radiation screens, since the opaque spacer material is optically thin very near the screens. Thus, the RTE was still used to calculate radiative heat transfer in the optically thick spacers,

$$\cos\theta \frac{dI}{ds} = -\beta I + \kappa n^2 I_b + \frac{\sigma}{2}\int_0^{\pi} I\left(\hat{\mathbf{s}}, \theta'\right)\sin\theta' d\theta' \tag{17}$$

In order to solve the RTE, the scaling model of Lee and Buckius [28, 29], which converts a scattering radiation problem into a non-scattering one, was used. In this elegant approach, the scattering coefficient is set to zero and the transmission and reflection coefficients are scaled, assuming linear scattering in an optically thin layer, as

$$\tau_{L,\beta} = \left(1-\omega\right)\tau_L; \quad and \quad \rho_\beta = 1 - \frac{2}{\frac{3}{4}\tau_L\omega + 2} \tag{18}$$

A further simplifying technique was to split up each layer of spacer material into *N* optically thin, isothermal layers, which are irradiated and emit radiation from both sides. In this manner, the transmittance, reflectance, and emittance of each layer were calculated independently and added together to yield the total radiative heat flux. The heat flux was then coupled to the energy equation in the solid via a source term,

$$\frac{d}{dx}\left[-k_c \frac{dT}{dx} + q_r\right] = 0 \tag{19}$$

The theoretical model predictions compared favorably with results in the literature for highly scattering materials, but not so well for purely absorbing materials.

2.4.3 Experimental results

The theoretical predictions were also compared to experimental data obtained by the authors [17, 18]. Test MTIs 30mm in thickness were constructed with screens (4 equally spaced) and without screens. The screens were stainless steel (Cr 22 A15Y), gold, or ceramic (Al_2O_3). The spacer materials tested were Isotherm 1000 (Frenzelit), HT 1000 (Klevers), Saffil (ICI), and Super G (Microtherm). Theoretical calculations of temperature dependent, effective thermal conductivity fit the experimental data within 10% except for the case of highly absorbing spacer materials.

In general, the presence of the screens dramatically lowers the effective thermal conductivity of the MTI, by as much as 50% in some cases. Also, it was shown that effective conductivity decreases with a decrease in screen emissivity (gold screens performed best). As expected, use of higher opacity spacer materials such as Microtherm Super G resulted in lower effective thermal conductivity. Overall, this work [17, 18] provides a sound theoretical and experimentally validated basis for the design and application of multi-layer thermal

insulation and can be recommended for use in design analysis of other thermal insulation materials for SOFCs.

2.4.4 Radiation from stack to environment

Effective stack thermal management is a requirement for maintaining uniform operating conditions across the stack and thus preserving stack efficiency. For example, if cells near the edge of the stack are not properly insulated, their performance can vary from the stack average causing variations in cell voltage. Heat loss from the edges also has the potential to induce damaging thermal gradients within cells. In addition, SOFC-based power plant design will require the outer surface of the insulation to be maintained at some safe, prescribed temperature [30]. These considerations make thermal modeling of the stack to environment critical, and because of high operating temperatures, thermal radiation should be given special treatment.

A first order simplifying approximation in modeling the stack would be to treat the outer surface of the stack as isothermal, exchanging heat with an isothermal inner surface of the insulation [30]. However, this is clearly not the case for some configurations of cells (co-flow, counter-flow), which exhibit highly non-isothermal behavior along the flow direction. It would be ideal to preserve this same temperature profile on the inner surface of the insulation, so as not to disturb the outer cells. In fact, a single cell can become completely isothermal if it is allowed to exchange thermal radiation with an isothermal enclosure [31]. This temperature non-uniformity would then propagate into the stack, affecting overall performance. Our literature review indicates that little has been reported about the interaction between stack and insulation and on the role of radiation heat transfer in minimizing heat losses from the stack. The methods for detailed treatment of radiation heat

transfer in stack thermal management have already been covered in this thesis and they are equally applicable to treatment of stack-to-environment radiation heat transfer. We can only emphasize again that the choice of the model and implementation will depend on the geometry, flow configuration and composition of the gas mixture, choice of insulating material, and prescribed external temperature of the insulation.

2.5 Concluding remarks

Radiation heat transfer in SOFC components and materials has been analyzed with a goal of developing the proper radiation modeling methods for different cases. Simplifying assumptions and simple scaling laws have been introduced, where applicable, to provide guidance and reduce costly computations. Radiation in participating media and surface-to-surface radiation exchange have been considered both within the unit cell and at the stack level. It was demonstrated that only careful treatment of these radiative regimes would enable an accurate prediction of temperature fields and operating conditions.

Measurements and analysis of spectral radiative heat transfer as relevant to SOFC membrane electrodes was reported. Specifically, the absorption coefficient and refractive index of the yttria-stabilized zirconia electrolyte (YSZ) were experimentally determined. It was found that the YSZ is optically thin for the electrolyte layer thicknesses relevant to currently developed SOFC, and optical properties exhibit strong wavelength dependence. The Schuster-Schwartzchild two-flux approximation was used to solve the RTE on a spectral basis with three spectral bands used to approximate spectral variation of the absorption coefficient. The model implementation was validated against an analytical solution from the literature for an isothermal case, as well as using the benchmark solution for one-dimensional

conduction-radiation heat transfer across gray and non-gray layers obtained using the discrete ordinate method implemented in the FLUENT CFD software.

It was found that for the geometry, materials, and operating conditions used in this study, which are thought as being representative of SOFC systems currently under development, radiative heat transfer within the electrolyte has negligible effect on the average cell operating temperature, voltage, or temperature gradients at the interfaces of the electrolyte and electrodes. In general, however, the geometry, materials, and operating conditions of SOFCs that will eventually be brought to market are unknown at this time. And because the spectral two-flux model is demonstrated to be an accurate and computationally-efficient method of accounting for radiative heat transfer within optically thin layers, it can and should be used as a part of any sound thermal-fluid analysis of SOFC systems.

We also reviewed thermal radiation heat transfer in the flow channels of SOFCs. Our analysis showed that the effect of participating gases is negligible due to the small dimensions of the channels (i.e. short optical path length which implies transparency of the medium). Surface-to-surface radiative heat flux is calculated through the Net Radiosity method. A key simplifying assumption is that the walls may be treated as black surfaces due to the high aspect ratio of the channels. A review of preliminary results in the literature shows that surface radiation effects result in a 0-30 ^{o}C difference in operating temperature as compared to the baseline case without radiation. In considering stack level radiative effects we discovered that, in light of recent developments, the design of high temperature thermal insulations is a fairly mature field. Stack thermal management, overall, presents its own set of challenges but the formulation of the radiative thermal models is well established.

CHAPTER 3

TRANSIENT HEAT TRANSFER ANALYSIS

3.1 Background

Solid oxide fuel cells (SOFCs) are currently being developed for mobile and stationary power plant applications, and much attention is being paid to the design and optimization of their steady state performance in an effort to make SOFC technology commercially viable in the near future. However, it is being increasingly realized [32] that because of substantial thermomechanical stresses developed in the cell components and stack, the transient process of heating an SOFC from room temperature to operating temperature (600 - 800 ^{o}C) during startup, or cooling down to ambient during shutdown must be given special attention as well. The ultra thin electrolyte and electrode layers (PEN structure) are prone to delamination, cracking, or other catastrophic failure if subjected to excessive thermal shock, temperature gradients, and thermal cycling during startup or shutdown processes.

These dangers can usually be avoided altogether by proceeding through the transient in a very slow, controlled fashion (in a recent ASME conference presentation Hawkes, et al., [33] reported taking two days to bring a stack up to operating temperature). As SOFC technology matures, however, it is likely that the consumer will demand that the fuel cell reach operating conditions as quickly as possible, for example, in the cold start of an automobile [30]. Thus, the optimal design of a startup process will minimize the total time required for heating, subject to the constraint of some maximum allowable temperature gradient (to avoid thermomechanical fracture) as well as time rate of change of temperature

(to avoid thermal shock and creep stresses). It will also be necessary to quantify the expected number of thermal cycles the cell can withstand during its lifetime, subject to the real possibility that faster heating times will lower the life expectancy of the cell.

In the literature, some preliminary efforts to address these concerns have been reported. Although numerous papers have presented the development of numerical/CFD models to simulate SOFC behavior at steady state, few are capable of simulating transient operation [22, 24, 30, 32], and only one [32] has begun to quantify thermally induced, transient thermal stresses during startup/shutdown. These models are based on finite element or volume approaches with the intent to give highly detailed information about current density, species distribution, flow and temperature fields, and propagation of thermal waves in the solid. Thus, the information required for transient design would be available, but the complexity of the models and the copiousness of the results may obscure the underlying physics of the process and prohibit the development of simple design rules for optimal transient heating/cooling processes (assuming such rules do exist). In addition, the rigorous CFD-based approaches demand a great deal of computational power, especially when simulating a long transient process with a large number of parameters to study. Adding to the computational expense is the very fine discretization required for numerical modeling because of the very high aspect ratio of components in the cell, for example, the 15 μm thick by 10 *cm* long electrolyte layer.

To overcome the above-mentioned conceptual and computational problems, we aim at developing reduced order models and an analytical approach leading to the closed-form solution of the problem. Our ultimate goal is to develop simple, efficient design rules that clearly show the effects of the various system parameters on 1) the total time required for

startup, and 2) the maximum temperature gradients developed during the process. The interest is not in developing a model that can give a highly detailed prediction of the temperature field at any given moment in time, but rather, a model that accurately and efficiently predicts the *global* quantities just mentioned. This work is the first to attempt to develop an efficient design strategy for optimizing the transient process and will focus on the initial startup of a cell from ambient temperatures with a simplified approach that generally (with few modifications) applies to shutdown as well.

3.2 Model formulation

Under consideration is the planar type SOFC, which is a stack of repeating unit cells with dimensions shown in Figure 14. The interconnects (current collectors) are made of stainless steel, the solid electrolyte is yttria-stabilized zirconia (YSZ), the porous anode is Ni-doped YSZ, and cathode is Sr-doped $LaMnO_3$ (LSM). The cell is heated by flowing hot air into the oxidizer channel while controlling the inlet air temperature as a function of time. As a first approximation, conditions in the fuel channel are assumed quiescent (negligible flow), with the composition of the gas phase similar to what would be found in a typical fuel stream. At startup, no electrochemical reactions take place until a prescribed temperature is reached, at which point electrochemical "light-off" occurs [34]. The electrochemical process generates heat, and consumes and produces chemical species in the flow streams, coupling the thermal-fluid model to the electrochemical model. For simplicity, it is assumed that a desired operating temperature is reached without triggering electrochemical reactions (i.e. no heat generation), so that attention is limited to convective heating of the cell.

Another simplifying assumption is that of a 1-D temperature field in each component of the cell, with variation only along the flow direction, as suggested by the high aspect ratio

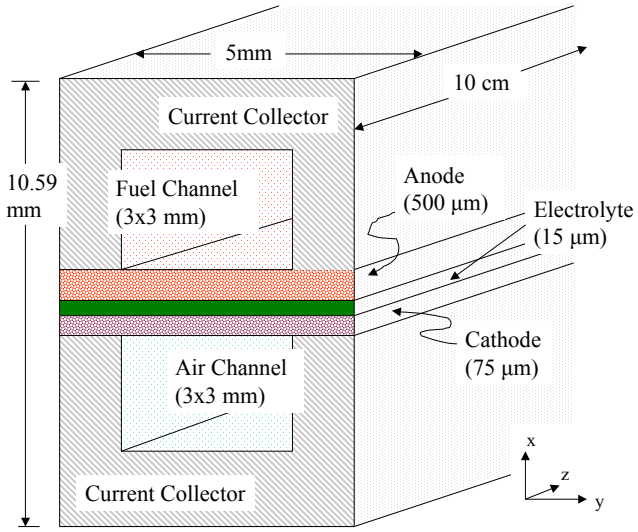

Figure 14. Geometry of the unit cell of a planar-type SOFC stack.

of the channel (>30:1). The small physical dimensions of the components also suggest that they may be in local thermal equilibrium (normal to the flow direction) and this possibility is investigated through the development and analysis of three reduced-order models of varying complexity. The first and most general model assumes the solid temperature is different from the gas temperature, and the resulting two-equation, coupled, transient model is solved numerically. The second model assumes the gas and solid are in local thermal equilibrium resulting in a single transient convective-conductive equation for which an analytical solution has been obtained [35]. The third model goes ones step further in simplifying the problem and assumes that conduction along the flow direction is negligible compared to advection of thermal energy down the length of the cell. This latter model is thus a purely convective heating model, also yielding an analytical solution. The range of validity of these models is then established by comparing their predictions of heating time and maximum temperature gradients to the results of detailed, 3-D CFD simulations of SOFC unit cell. It is assumed that the geometry of the cell, material selection, and initial and final temperatures are

prescribed design parameters, leaving the inlet air temperature and air velocity (flow rate) as parameters that can be used to optimize the heating process.

3.2.1 Two-equation, coupled, solid-gas model

The most general, reduced order, transient heating model we developed is derived by applying conservation of energy to each layer (component) of the cell shown in Figure 15. This yields a set of seven partial differential equations (PDEs) that are coupled through the temperature difference between adjoining layers. The equation for the air channel, assuming constant velocity plug flow and neglecting thermal radiation, is

$$\left(\rho c_p A\right)_g \left[\frac{\partial T_g}{\partial t} + u\frac{\partial T_g}{\partial z}\right] = \left(kA\right)_g \frac{\partial^2 T_g}{\partial z^2} - hP_{g-C}\left(T_g - T_C\right) - hP_{g-IC}\left(T_g - T_{IC}\right) \qquad (20)$$

subject to the boundary and initial conditions,

$$\begin{aligned} &\underline{B.C.'s}: \quad T_g\left(0,t\right) = f\left(t\right); \quad \frac{\partial T_g}{\partial z}\left(L,t\right) = 0 \\ &\underline{I.C.}: \quad\quad T_g\left(z,0\right) = T_o \end{aligned} \qquad (21)$$

where, h is the convective heat transfer coefficient, T_C and T_{IC} are temperatures of the

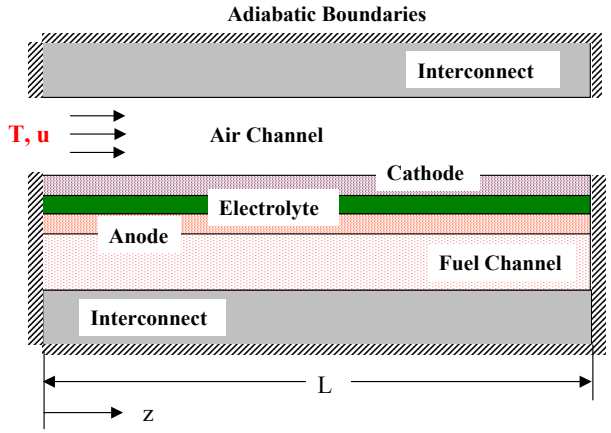

Figure 15. Schematic of the unit cell as a channel with composite, insulated walls. The temperature profile is assumed 1-D in each layer with variation in the flow, z-direction only.

cathode and interconnect, respectively, P_{g-C} and P_{g-IC} are the contact perimeters between the air (gas) channel and the cathode layer , and the air (gas) channel and the interconnect layer, respectively, A is the cross sectional area of the air channel, and k, ρ, c_p are the thermal conductivity, density, and specific heat of the air, respectively. Similar equations are written for the other layers, for example, the interconnect layer,

$$\left(\rho c_p A\right)_{IC} \frac{\partial T_{IC}}{\partial t} = \left(kA\right)_{IC} \frac{\partial^2 T_{IC}}{\partial z^2} + hP_{g-IC}\left(T_g - T_{IC}\right) - \frac{P_{IC-C}}{R_{IC-C}}\left(T_{IC} - T_C\right) \qquad (22)$$

which is coupled to the air equation through the convection term (the second term on the right-hand-side), and to the cathode layer (see Figures 14 and 15) through the thermal resistance,

$$R_{IC-C} = \frac{t_{IC}}{2k_{IC}} + \frac{t_C}{2k_C} \qquad (23)$$

where, t_{IC}, t_C are the thickness of the interconnect and cathode layers, respectively. In like manner, the remaining equations for the cathode (*C*), electrolyte (*E*), anode (*A*), fuel channel (*f*), and lower interconnect (IC_2), are,

$$\begin{aligned}
\left(\rho c_p A\right)_C \frac{\partial T_C}{\partial t} &= \left(kA\right)_C \frac{\partial^2 T_C}{\partial z^2} + hP_{g-C}\left(T_g - T_C\right) + \frac{P_{IC_1-C}}{R_{IC-C}}\left(T_{IC} - T_C\right) - \frac{P_{C-E}}{R_{C-E}}\left(T_C - T_E\right) \\
\left(\rho c_p A\right)_E \frac{\partial T_E}{\partial t} &= \left(kA\right)_E \frac{\partial^2 T_E}{\partial z^2} + \frac{P_{C-E}}{R_{C-E}}\left(T_C - T_E\right) - \frac{P_{E-A}}{R_{E-A}}\left(T_E - T_A\right) \\
\left(\rho c_p A\right)_A \frac{\partial T_A}{\partial t} &= \left(kA\right)_A \frac{\partial^2 T_A}{\partial z^2} + \frac{P_{E-A}}{R_{E-A}}\left(T_E - T_A\right) - hP_{f-A}\left(T_f - T_A\right) - \frac{P_{A-IC_2}}{R_{A-IC_2}}\left(T_A - T_{IC_2}\right) \qquad (24) \\
\left(\rho c_p A\right)_{fuel} \frac{\partial T_{fuel}}{\partial t} &= \left(kA\right)_{fuel} \frac{\partial^2 T_{fuel}}{\partial z^2} + hP_{f-A}\left(T_f - T_A\right) + hP_{f-IC_2}\left(T_f - T_{IC_2}\right) \\
\left(\rho c_p A\right)_{IC_2} \frac{\partial T_{IC_2}}{\partial t} &= \left(kA\right)_{IC_2} \frac{\partial^2 T_{IC_2}}{\partial z^2} + \frac{P_{A-IC_2}}{R_{A-IC_2}}\left(T_A - T_{IC_2}\right) - hP_{f-IC_2}\left(T_f - T_{IC_2}\right)
\end{aligned}$$

The boundary and initial conditions for Eqs. (22) and (24) are all of the same form,

$$\underline{B.C.'s}: \quad \frac{\partial T_i}{\partial z}(0,t) = \frac{\partial T_i}{\partial z}(L,t) = 0; \quad \underline{I.C.}: \quad T_i(z,0) = T_o \tag{25}$$

This set of coupled PDEs can be solved numerically in its current form, but a reasonable simplifying assumption at this point, is that the temperatures in the solid are locally uniform at each cross-section in the direction normal to the flow. This is verified by calculating the Biot number, *Bi*, for this configuration as the ratio of thermal resistance across the entire composite channel wall, to convective thermal resistance between the channel walls and air stream,

$$Bi = \frac{R_{conduction}}{R_{convection}} = h\sum_i \frac{t_i}{k_i} \tag{26}$$

where h is the convection heat transfer coefficient, t is the thickness of layer i and k is thermal conductivity. Using values found in Table 3 for k_i, dimensions from Figure 14 for t_i, and estimating $h \sim 60\ Wm^{-2}K^{-1}$ for fully-developed internal, laminar air flow in a 3 *mm* pipe, yields $Bi \sim 0.02$, validating the assumption that the solid can be treated as a locally isothermal lumped capacitance element. This understanding allows us to combine Eqs. (22) and (24) to formulate a single energy equation for the effective temperature of the solid matrix,

$$\sum_i \left(\rho c_p A\right)_i \frac{\partial T_s}{\partial t} = \sum_i (kA)_i \frac{\partial^2 T_s}{\partial z^2} + hP_{g-s}\left(T_g - T_s\right) \tag{27}$$

with boundary and initial conditions,

$$\underline{B.C.'s}: \quad \frac{\partial T_s}{\partial z}(0,t) = \frac{\partial T_s}{\partial z}(L,t) = 0; \quad \underline{I.C.}: \quad T_s(z,0) = T_o \tag{28}$$

The equation for the gas is similar to Eq. (20),

$$\left(\rho c_p A\right)_g \left[\frac{\partial T_g}{\partial t} + u\frac{\partial T_g}{\partial z}\right] = \left(kA\right)_g \frac{\partial^2 T_g}{\partial z^2} + hP_{g-s}\left(T_s - T_g\right) \tag{29}$$

with the same boundary and initial conditions given in Eq. (21). We further consider the case when the inlet air temperature is defined by a linear increase in time until a desired final (T_f) steady-state temperature is reached,

$$f\left(t\right) = \begin{cases} T_o + Kt & t \le \left(T_f - T_o\right)/K \\ T_f & t > \left(T_f - T_o\right)/K \end{cases} \tag{30}$$

where, K is the rate of temperature rise at the inlet in units of $^oC\ s^{-1}$. It should be noted that although the results for the linear temperature increase are discussed in this thesis, all mathematical developments are general and could be readily extended in a straight-forward fashion to investigate any functional dependence of the inlet air temperature.

Equations (27) and (29) are solved numerically using a Crank-Nicholson, finite difference scheme [36] (see Appendix B for details). The gas equation for the next future time step is solved by guessing a temperature distribution in the solid, and using the tri-diagonal matrix algorithm [36] to invert the coefficient matrix. Using this temperature distribution, the solid equation is solved in a similar manner, and the process is repeated until

Table 3. Material Properties of Cell Components

Component	$\rho\left(\frac{kg}{m^3}\right)$	$k\left(\frac{W}{m\,K}\right)$	$c_p\left(\frac{J}{kg\,K}\right)$
Anode (Ni-doped YSZ)	3030	5.84	595
Cathode (LSM)	3310	1.86	573
Electrolyte (YSZ)	5160	2.16	606
Current collector (SS)	8030	20.0	502
Air Channel	0.58	0.047	1051
Fuel Channel	0.2	0.2	5000

the temperatures converge before proceeding to the next time step. The calculations proceed forward in time until steady-state is reached. Temperature gradients (spatial and temporal) are calculated numerically from the resulting temperature field history, allowing the maximum temperature gradients developed through the entire heating process to be identified. The only modification necessary for simulating cooling (rather than heating) processes is to use negative values for K in the boundary condition, Eq. (30).

3.2.2 Convective-conductive model

To further simplify Eqs. (27) and (29), and to enable closed-form analytical solution of the problem, an assumption of local thermal equilibrium between the gas and solid is employed. This bold simplification is applied to the problem at hand, not to prove or disprove that the solid and gas are at the same temperature, but to determine whether the approach will yield accurate predictions of heating time and maximum temperature gradients. If the model can accomplish this task, and do it analytically, then it is a very powerful design tool for optimizing the transient heating and cooling process.

To implement the local thermal equilibrium assumption correctly (i.e., without even locally violating energy conservation), the following procedure is employed: First, both conservation equations (27) and (29) are added together, which cancels the coupling convective solid-gas heat exchange term. Then, by definition of local thermal equilibrium, the temperatures of the gas and solid are made the same, leading to the following single convective-conductive governing equation describing transient heating dynamics of the unit cell:

$$\frac{\partial T}{\partial t} + u_{eff} \frac{\partial T}{\partial z} = \alpha_{eff} \frac{\partial^2 T}{\partial z^2} \tag{31}$$

where, u_{eff} is the *effective* velocity and α_{eff} is the *effective* thermal diffusivity defined as follows,

$$u_{eff} = \frac{\left(\rho c_p A\right)_g}{\sum_i \left(\rho c_p A\right)_i} \cdot u \; ; \quad \alpha_{eff} = \frac{\sum_i \left(kA\right)_i}{\sum_i \left(\rho c_p A\right)_i} ; \tag{32}$$

Note that the summations are now indexed to include every component of the cell including flow channels. The effective velocity is the physical air velocity scaled by the ratio of heat capacity of the air channel to energy stored in the channel walls. The effective thermal diffusivity is the cross-sectional area-weighted diffusivity of the composite channel wall. Both of these terms are dominated by the relatively massive interconnects with their high conductivity, density, and cross-sectional area.

The same procedure used to derive Eq. (31) can be applied to the boundary and initial conditions (they must be first expressed in a conservative basis in terms of the total energy rate/flux [35]), yielding,

$$\begin{aligned} &\underline{B.C.'s}: \quad T\left(0,t\right) - \beta_{eff} \frac{\partial T}{\partial z}\left(0,t\right) = f\left(t\right); \quad \frac{\partial T}{\partial z}\left(L,t\right) = 0 \\ &\underline{I.C.}: \qquad T\left(z,0\right) = T_o \end{aligned} \tag{33}$$

where the coefficient β_{eff} in Eq. (33) combines thermal energy conduction in the solid to thermal energy transport in the air channel,

$$\beta_{eff} = \frac{\left(kA\right)_{IC_1} + \left(kA\right)_C + \left(kA\right)_E + \left(kA\right)_A + \left(kA\right)_f + \left(kA\right)_{IC_2}}{\left(\rho c_p A\right)_g u} \tag{34}$$

Notice that if heat diffusion in the air is neglected—a very reasonable approximation as compared to advection—then, $\beta_{eff} = \alpha_{eff} / u_{eff}$.

When temperature, length, and time are normalized using the following characteristic scales,

$$T^* = \frac{T - T_o}{T_f - T_o}; \quad z^* = \frac{z}{L}; \quad t^* = \frac{t}{\left(L / u_{eff}\right)} \tag{35}$$

the dimensionless form of Eq. (31) can be expressed as,

$$\frac{\partial T^*}{\partial t^*} + \frac{\partial T^*}{\partial z^*} = \frac{1}{Pe}\frac{\partial^2 T^*}{\partial z^{*2}} \tag{36}$$

where Pe is defined as the *effective* Peclet number, $Pe = u_{eff} L / \alpha_{eff}$, that is, the ratio of advection of thermal energy down the length of the channel to diffusion of thermal energy in the solid layers of the SOFC unit cell. Likewise, the boundary and initial conditions are

$$\begin{aligned} &\underline{B.C.'s}: \quad T^*\left(0, t^*\right) - \frac{1}{Pe}\frac{\partial T^*}{\partial z^*}\left(0, t^*\right) = F\left(t^*\right); \quad \frac{\partial T^*}{\partial z^*}\left(1, t^*\right) = 0 \\ &\underline{I.C.}: \qquad T^*\left(z^*, 0\right) = 0 \end{aligned} \tag{37}$$

where $F\left(t^*\right)$ is the non-dimensional form of the inlet temperature function given by Eq. (30)

$$F\left(t^*\right) = \frac{KL}{\left(T_f - T_o\right) u_{eff}} t^* \tag{38}$$

Eq. (38) reveals the second dimensionless parameter that determines the thermal response of the cell, the *effective* rate of inlet temperature rise,

$$K_{eff} = \frac{L / u_{eff}}{\left(T_f - T_o\right) / K} \tag{39}$$

Physically, this parameter represents the ratio of the advective time scale, $\tau_c = L / u_{eff}$, to the time scale associated with the transient forcing of the inlet temperature, $\tau_i = \left(T_f - T_o\right) / K$, that is, the time required for the inlet air temperature to reach the final desired temperature. A significant insight into the transient heating process can be obtained by analyzing this

parameter. In advection dominated flows ($Pe >> 1$, note the modified definition of effective Peclet number here, combining properties of the air and solid), a value of K_{eff} greater than unity implies that the rate of thermal energy input at the inlet of the cell exceeds the capability of the cell to store and distribute this heat input. Thus, temperature at the inlet builds up too quickly, leading to excessive thermal gradients without significant improvement in total heating time.

The usefulness of Eq. (36) lies in the fact that a closed-form analytical series solution has been found [35] (see Appendix C for details), and that the temperature distribution dependence has been reduced to only two dimensionless parameters: effective Peclet number, Pe, and the effective rate of inlet temperature rise, K_{eff}. Also, this solution provides a convenient way to validate the numerical scheme used to solve Eqs. (27) and (29) in Section 3.2.1. As the heat transfer coefficient coupling the gas and solid temperatures is made arbitrarily large, the temperatures of the gas and solid should converge onto each other and the resulting single temperature solution must match the analytical result given by the closed-form solution of Eq. (36).

3.2.3 Purely convective model

A very interesting limiting case of Eq. (36) is that of purely convective flow ($Pe \to \infty$), in which case the right-hand side of Eq. (36) vanishes. The resulting equation,

$$\frac{\partial T^*}{\partial t^*} + \frac{\partial T^*}{\partial z^*} = 0 \tag{40}$$

and in particular, its dimensional form,

$$\frac{\partial T}{\partial t} + u_{eff} \frac{\partial T}{\partial z} = 0 \tag{41}$$

looks very much like the governing equation for a cell with thermally thin cell components (i.e. no thermal energy storage in cell components, and local thermal equilibrium between the solid and gas [35]). However, because the *effective*, not physical velocity is used here, thermal energy storage in the cell is properly accounted for, and only thermal energy conduction along the axial direction is neglected. The relevant boundary and initial conditions are, respectively,

$$T^*\left(0,t^*\right)=F\left(t^*\right);\quad T^*\left(z^*,0\right)=0\,. \tag{42}$$

The method of characteristics yields the analytical solution of the time dependent, 1-D temperature distribution:

$$T^*\left(z^*,t^*\right)=\begin{cases}0, & z^*>t^*\\ K_{eff}\left(t^*-z^*\right), & z^*\le t^*\end{cases} \tag{43}$$

This very simple equation for the unsteady temperature distribution provides simple algebraic relationships for dimensionless heating time

$$\tau_h^*=1/K_{eff}+1 \tag{44}$$

and dimensionless temperature gradients

$$-\left.\frac{\partial T^*}{\partial z^*}\right|_{\max}=\left.\frac{\partial T^*}{\partial t^*}\right|_{\max}=K_{eff} \tag{45}$$

The dimensional form of these equations yields some physical insight. The total heating time is the sum of the two time scales, τ_c and τ_i previously discussed in Section 3.2.2 above,

$$\tau_h=\frac{T_f-T_o}{K}+\frac{L}{u_{eff}} \tag{46}$$

The fastest that the cell can be heated, assuming it is a perfect heat exchanger, is given by the time required to bring the incoming air to the desired operating temperature, plus the time

required for thermal energy to travel from the inlet to the exit. So, Eq. (46) is the theoretical lower bound (minimum possible value) on heating time, and unambiguously suggests that heating time is inversely proportional to both K and u. The maximum dimensional (physical) temperature gradients become,

$$-\left.\frac{\partial T}{\partial z}\right|_{\max} = \frac{K}{u_{eff}}; \quad \left.\frac{\partial T}{\partial t}\right|_{\max} = K \tag{47}$$

indicating that spatial temperature gradient is inversely proportional to u, but both temperature gradients (spatial and temporal) increase linearly with K. Equations (47) set upper bounds on the maximum temperature gradients that can exist in the solid during the transient heating, owing to the fact that thermal conduction, which tends to diminish temperature gradients, has been neglected in the formulation.

Equations (46) and (47) constitute very simple design rules that establish relationships between design parameters and clearly explain the competing effects that must be balanced to optimize the heating process:

- Increasing flow velocity, u, tends to decrease both the heating time (*positive effect*) and spatial temperature gradient (*positive effect*), but has no effect on the temporal gradient.
- Increasing the rate of inlet temperature rise, K, tends to decrease the required heating time (*positive effect*), but increases both the temporal and spatial temperature gradients (*negative effect*).

Thus, the purely convective model has yielded useful information about limiting cases, which in hindsight seems to be almost intuitively obvious, and provides the framework for optimization of the heating process—even though the validity of the results still needs to be established. This is done in the next section. In order to determine whether or not the simple,

reduced-order transient heating models have any significant bearing on reality, we compared their predictions of heating time and temperature gradients to the results of transient 3-D CFD simulations of SOFC unit cell heating.

3.2.4 CFD model

To critically compare the predictive power of the reduced-order transient thermal models, a fully three-dimensional thermal-fluid analysis of the unit cell in Figure 14 was performed via the commercially available CFD software Fluent. In simulations, thermophysical properties of the solid materials were assumed constant (estimated at the average temperature) and are listed in Table 3. The steady-state flow field in the oxidizer channel was found under the assumption of laminar flow using constant thermophysical fluid properties evaluated at the average temperature of 300 °*C*. For simplicity, this flow field was then used for the unsteady calculations of the temperature field in the cell, as the inlet temperature was linearly increased from 25 to 625 °*C*. Once the inlet air temperature reached 625 °*C*, it was held constant until the normalized temperature of the solid at the end of the flow channel was within 5% of the normalized steady state value (i.e. 595 °*C*), at which point the simulations were terminated. The temperature history of the solid (electrolyte) was recorded throughout, and post-processed to yield maximum spatial and temporal temperature gradients. Because of symmetry along the axial midplane, only half of the unit cell was modeled using 44,000 discrete volumes. The mesh and time-step were properly refined to ensure that the results were mesh and time-step independent. The time-step for each simulation was adjusted based on the rate of inlet temperature rise, *K*, and typically corresponded to a 2 °*C* (per time step) temperature rise at the inlet.

Cases were run for K values of 0.01, 0.02, 0.05, 0.1, 0.2, 0.5, 1.0, and 2.0 $°C$/s. The inlet velocities used were, 1, 5, 10, and 20 *m*/*s*, corresponding to effective Peclet numbers of 0.8, 4.2, 8.4, and 16.7. Results of these simulations are compared with results of the reduced-order models in the next section.

3.3 Model results and analysis

First, the results of CFD simulations were compared to predictions obtained with the most general reduced-order model, which is the two-equation, coupled, solid-gas model described in Section 3.2.1. Before the two-equation model can be numerically solved, the heat transfer coefficient, h, must be specified at each point along the air channel. Because almost one-third of the channel is in the thermally-developing entrance region, the correlation based on the Graetz solution for thermally developing, hydrodynamically fully-developed laminar flow in a duct with constant wall temperature [37] was used to approximately account for variation in heat transfer coefficient along the channel length:

$$Nu_x = 3.66 + \frac{0.0018}{x^{*1/3}\left(0.04 + x^{*2/3}\right)^2}; \qquad x^* = \frac{x/D_h}{\mathrm{Re}\,\mathrm{Pr}} \tag{48}$$

where the Nusselt number at a given position, x, is $Nu_x = h_x D_h / k$, hydraulic diameter is $D_h = 4A_c / P_w$, the Reynolds number is $\mathrm{Re} = uD_h / \eta$ and Prandtl number is $\mathrm{Pr} = \eta / \alpha$.

Several steps were taken to validate the numerical solution of the two-equation, coupled, solid-gas model, Eqs. (27) and (29). First, the grid spacing was reduced until results were grid independent. This requirement was satisfied by discretizing the channel length into 100 nodes. Second, the time step was reduced until results were time-step independent,

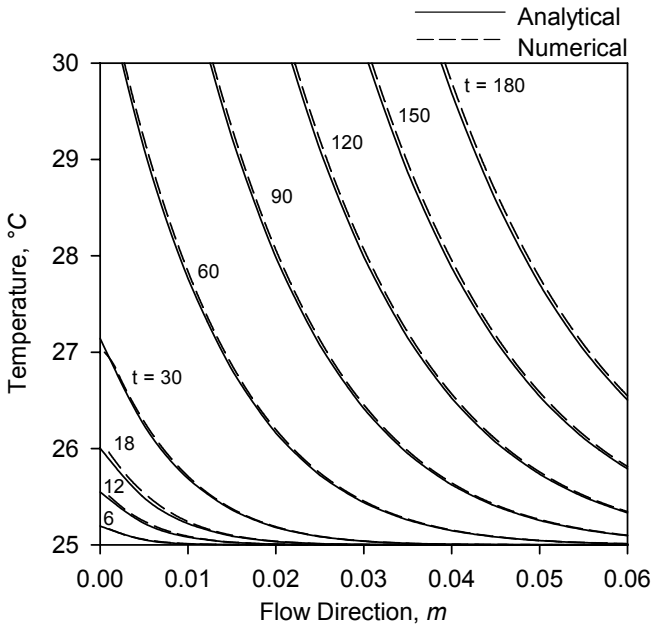

Figure 16. Validation of numerical solution of two-equation, coupled solid-gas model (dashed line) vs. analytical solution of convective-conductive model (solid line) in the limit of local thermal equilibrium. The cell is in the initial stages of being heated by hot air with velocity, $u = 1$ *m*/*s*, and at a rate $K = 1$ °*C*/*s*. Simulation time (in seconds) for each temperature profile is indicated as a label for each curve in the figure.

which occurred for the same time-step size as discussed in Section 3.2.4 for the CFD model. Finally, the numerical solution was validated against the analytical solution of the 2nd reduced-order model in Section 3.2.2 in the limit of local thermal equilibrium. In order to force thermal equilibrium between the gas and solid, the heat transfer coefficient was made 1000 times larger than the baseline, thermally-fully developed value ($x^* \to \infty$) for laminar flow in a duct as predicted by Eq. (29). This caused the temperature difference between the gas and solid to vanish, and the resulting solid/gas temperature profile matched that obtained analytically by solving Eq. (31). Figure 16 shows results of this validation test for a cell in the initial stages of being heated by air flowing at $u = 1$ *m*/*s* with the inlet air temperature increasing at a rate of $K = 1$ °*C*/*s*. The analytical and numerical solutions match very well for this case as well as several other cases that were run, thus establishing the validity of the numerical procedure used for integration of the 1st reduced-order model, Eqs. (27) and (29). .

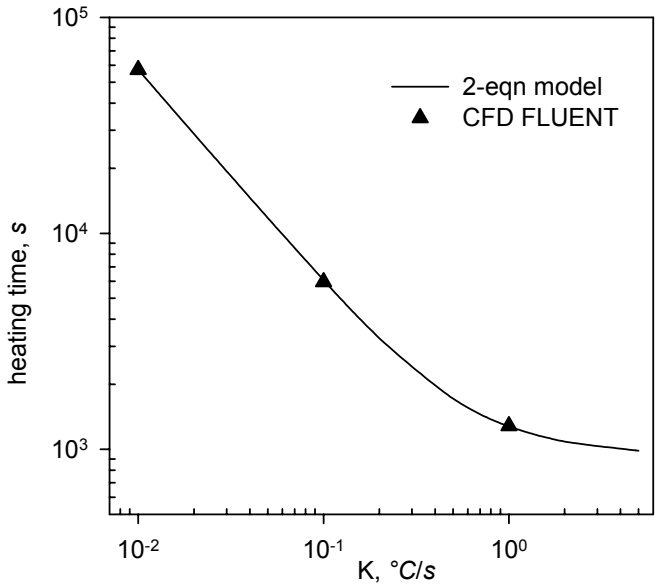

Figure 17. Predictions of heating time vs. K for hot air velocity, u = 10 m/s. The solid line is the two-equation, coupled, solid-gas model predictions, and the triangles are data points obtained from 3-D CFD Fluent simulations.

Having validated the numerical scheme for solving the two-equation coupled, solid-gas model, the predictions of heating time and maximum temperature gradient were compared to the results of the CFD Fluent simulations. Figures 17 and 18 show heating time, spatial temperature gradient, and temporal temperature gradient vs. rate of inlet temperature rise, K, for a heating air velocity of u = 10 m/s. The predictions of heating time and temporal temperature gradient show excellent agreement for a wide range of K. However, the model significantly over predicts spatial temperature gradients (>100% error) as seen in Figure 18. In fact, this was seen to be the case for most values of u that were used in simulations. Further investigation revealed that the excessive temperature gradients occurred near the inlet and were highly sensitive to the assumed behavior of heat transfer coefficient, h, which increases dramatically near the inlet. Indeed, the constant-wall temperature correlation, Eq. (48), appeared to predict significantly larger values of h (near the inlet) than what was found by rigorous solution of the conjugate mass, momentum, and energy conservation equations in

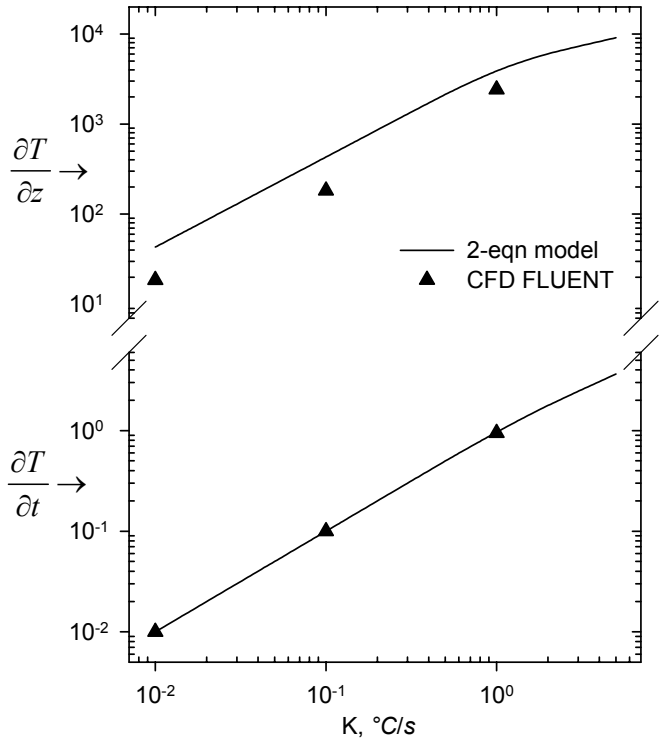

Figure 18. Predictions of maximum temperature gradient vs. K for hot air velocity, $u = 10$ m/s. The solid line is the two-equation, coupled, solid-gas model predictions, and the triangles are results of 3-D CFD Fluent simulations. The upper plot is for spatial temperature gradient and the lower plot is for temporal temperature gradient.

the Fluent CFD model. In reality, h varies with air velocity, distance from the inlet, thermal condition of the channel walls, and time—a relationship not explicitly known, and requiring solution of a much more complicated conjugate heat transfer problem (see for example, [38, 39]). Adding this significant additional level of complexity to the two-equation coupled solid-gas model would cut into its expected advantage of being much simpler and more computationally efficient than the 3-D Fluent model.

Having established that the two-equation coupled solid-gas numerical model is severely limited in its ability to be used as a reliable transient process design tool for SOFCs, the remainder of our analysis will focus on the analytical model results and their application to optimal design of SOFC transient heating process. These two analytical reduced-order

models—for purely convective and convective-conductive heating—were solved for a range of realistic values of effective rate of inlet temperature rise, K_{eff}, and effective Peclet number, *Pe*. All calculations were performed for the SOFC geometry shown in Figure 14 and the material property values given in Table 3. The studied values of *Pe* correspond to physical velocity in the range $1 \le u \le 20\, m/s$, and the values of K_{eff} covers the range $0.01 \le K \le 5\ \ ^{\circ}C/s$ in terms of the actual rate *K* of the inlet air temperature rise. Model predictions of dimensionless heating time, and maximum temperature gradients (spatial and temporal) are shown in Figures 19 through 21. Strictly speaking, the purely convective model is the limiting case of the convective-conductive model, in the limit of $Pe \to \infty$. However, the convective-conductive model results rapidly converge to the purely convective

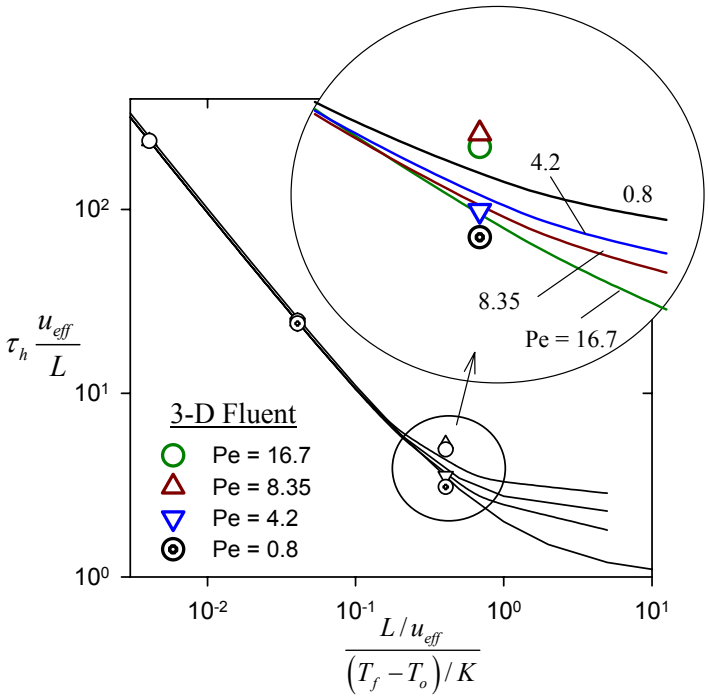

Figure 19. Dimensionless heating time, τ_h^*, as a function of K_{eff} for various effective Peclet numbers. The solid lines are the reduced-order analytical model predictions and the data points are results of 3-D Fluent simulations. For $K_{eff} \ll 1$ the analytical models (regardless of Peclet number) accurately predict heating time. As K_{eff} increases, the analytical models are less accurate but still predict the correct trend. For large Peclet numbers (e.g. *Pe* = 16.7) both analytical models (i.e., for purely convective and convective-conductive heating) predict identical results.

model results for effective Peclet numbers as small as 10. Thus, the results for the case of *Pe* = 16.7 shown in the plots are obtained using the purely convective model calculations with the realization that further increases in *Pe* do not change the behavior.

3.3.1 Heating time

The first quantity of interest in transient thermal modeling of SOFCs is the total time required to heat the cell to the desired operating temperature. Figure 19 shows total dimensionless heating time for various K_{eff}. The dimensionless heating time predicted by the purely convective reduced-order model is simply $\tau_h^* = 1/K_{eff} + 1$, which is a much 'nicer' result than the infinite series solution of the convective-conductive model. However, it is apparent from Figure 19 that the convective-conductive model and the purely convective model give virtually indistinguishable results for any (even small) *Pe* as long as K_{eff} is sufficiently small. At larger K_{eff}, some *Pe* dependence is seen, with heating time asymptotically approaching a finite value (dimensionless value greater than 1) depending on *Pe*. Another feature of Figure 19 is that excellent agreement (<2% error) is obtained between the analytical models and 3-D Fluent simulation results at small values of effective rate of inlet temperature rise, $K_{eff} \sim< 0.1$. This lack of *Pe* dependence and good agreement with rigorous CFD simulations is hardly surprising when considered in the context of the physical time scales, τ_c and τ_i, identified in Section 3.2.2 of this paper. Small K_{eff} implies that the time scale associated with the prescribed rate of inlet temperature rise, $\tau_i = \left(T_f - T_o\right)\big/K$, is primarily responsible for determining how fast the cell can be heated. Thus, with respect to predictions of total heating time, the details of heat transfer within the cell are practically

irrelevant! (The relevant portion of the analysis was implicitly included in the statement that K_{eff} is small.) For large K_{eff} this is no longer the case; the time scale (and mechanism) for heat flow within the channel (whether by advection or conduction) is of critical importance, and a rigorous multi-dimensional thermal-fluid analysis is required in order to accurately predict heating time. Fortunately, K_{eff} (as related to SOFC unit cells) is often small, and use of the purely convective model for prediction of heating time is quite accurate for practical purposes.

3.3.2 Maximum spatial temperature gradient

The second quantity of interest in transient thermal modeling of SOFCs is maximum spatial temperature gradient, which sets an upper limit on thermomechanical stress developed in the cell during its transient heating. The purely convective model prediction of

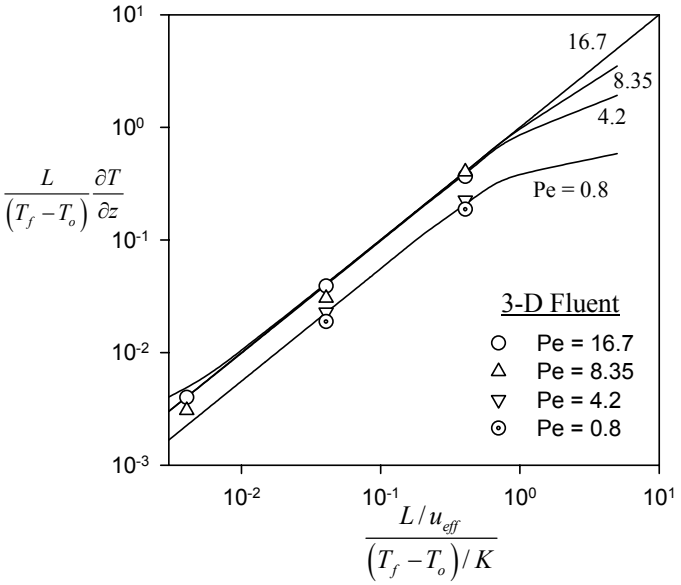

Figure 20. Maximum dimensionless spatial temperature gradient as a function of K_{eff} for various Peclet numbers. The solid lines are the analytical convective-conductive model predictions and the data points are results of 3-D Fluent simulations. Temperature gradients decrease with a decrease in *Pe* at a fixed K_{eff}. The case of *Pe* = 16.7 is as calculated from the purely convective model (the limiting case of $Pe \to \infty$), which yields results identical to those obtained using the convective-conductive model at such a high Peclet number.

dimensionless maximum temperature gradient is explicitly stated in Eq. (47). On the other hand, convective-conductive model predictions of temperature gradient were calculated numerically from the analytical solution of Eq. (36). Results of these two models along with predictions obtained using the 3-D Fluent simulations are shown in Figure 20. Satisfactory agreement between the models (<20% error) is seen at high effective Peclet numbers ($Pe \geq 8$) for $K_{eff} \sim < 1$. It is clear that the purely convective model over predicts temperature gradients for very low *Pe*, although it still predicts the correct trends. The convective-conductive model provides some improvement at very low *Pe*, but it is not reliable for intermediate values. An expected, yet interesting feature of the graphs shown in Figure 20 is that the dimensionless temperature gradient for any given K_{eff} decreases with a decrease in *Pe* from its maximum at large *Pe* values (purely convective model). This is due to the fact that the addition of conduction as a significant heat transfer mechanism reduces temperature gradients along the axial direction. This does not imply, however, that real (physical) temperature gradients decrease with a decrease in velocity. The only way that lowering the effective Peclet number will result in lower (real) temperature gradients is by increasing the effective thermal diffusivity of the cell. Unfortunately, this may not be a viable design option, as it requires changing the geometry of the cell or selecting new materials, which are usually optimized for the most efficient steady-state operation.

3.3.3 Maximum temporal temperature gradient

One last quantity of interest in transient operation of a cell is the maximum temporal temperature gradient in cell materials. This is important because the cell is composed of layers made of different materials with different thermal expansion coefficients and

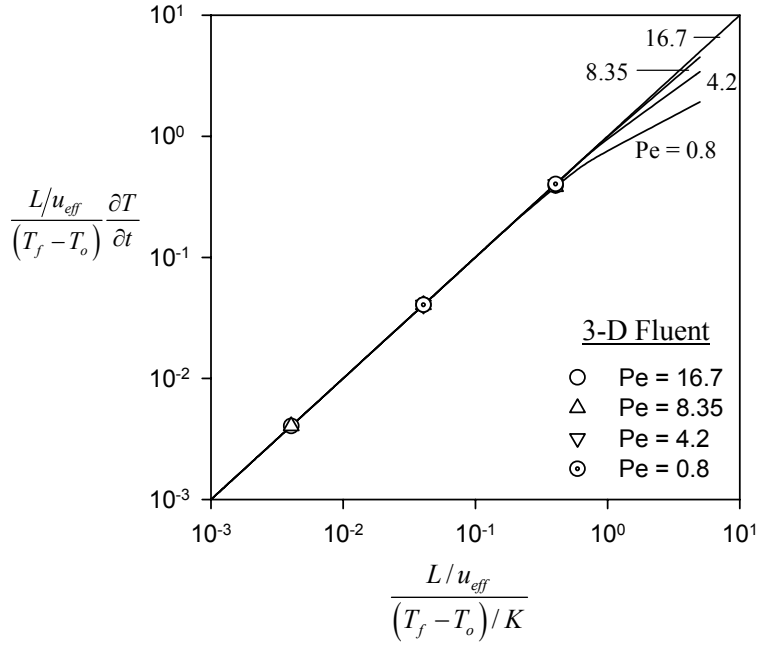

Figure 21. Maximum dimensionless temporal temperature gradient as a function of K_{eff} for various Peclet numbers. The solid lines are the analytical model predictions and the data points are results of 3-D Fluent simulations. Excellent agreement between the analytical models and 3-D results is observed across a wide range of K_{eff}. At values of K_{eff} <~ 0.5 the Peclet dependence is negligible and the purely convective heating analytical model provides satisfactory results.

characteristic time scales for creep. If the temporal temperature gradient exceeds the rate at which creep can relax interfacial stress due to thermal expansion mismatch, then delamination, cracking, or other failure may occur. Figure 21 is a plot of the maximum dimensionless temporal temperature gradient for various *Pe* and K_{eff}. Clearly, for the values of K_{eff} less than ~1, the temporal gradient is essentially independent of *Pe*, showing excellent agreement with the 3-D Fluent model results. Thus, results given by the purely convective heating model are valid for prediction of the local rate of temperature change during transient heating of the SOFC.

For the three global quantities of interest—heating time, maximum spatial temperature gradient, and maximum temporal temperature gradient—we find then, that the

purely convective model provides satisfactory results within certain limits of parameters. For heating time predictions, the model is valid for $K_{eff} \leq 0.1$ and $1 \leq Pe \leq \infty$. The purely convective model may be valid at even smaller effective Peclet numbers, but we do not have data to support this, and do not envision scenarios in which such low *Pe* is a realistic operating regime. For maximum spatial temperature gradients, the model is reasonably accurate for $K_{eff} \leq 1$ and $5 \leq Pe \leq \infty$. If in-depth, precise local information, beyond simply the maximum temperature gradient, is required, we recommend multi-dimensional, CFD modeling such as that described in Section 3.2.4. The purely convective heating model is also valid for predicting maximum temporal temperature gradients in the ranges $K_{eff} \leq 1$ and $1 \leq Pe \leq \infty$. Because the convective-conductive model provides little improvement for expanding this range of validity, we recommend a design procedure for the heating/cooling process based on the purely convective model only. Note that this model is shown to have good predictive capabilities for the global heating/cooling characteristics just mentioned, and not necessarily for giving detailed time-varying temperature fields within the cell.

3.4 Design maps for heating and cooling

Figures 19 through 21 are design maps, which can be used to develop a protocol for an optimal SOFC heating process. Typically, the cell geometry and material selection will be optimized for steady-state cell performance, leaving the hot air velocity, *u*, and heating rate, *K*, as control variables for optimizing the transient process. Assuming that the maximum allowable stress (and corresponding temperature gradient) has been specified through a thermo-mechanical stress analysis of the unit cell, the design goal is to minimize heating time through proper choice of *K* and *u*. One method for using these design maps is as follows: First, fix the effective velocity at the maximum value allowed by system constraints (cell

geometry, materials, pumping power, etc.). (The reason for choosing the highest possible velocity will become apparent shortly.) This will fix the effective Peclet number since cell geometry and materials are not likely to be variable. Next, specify a maximum allowable spatial temperature gradient below which no thermo-mechanical failure would be expected to occur. Using this value, together with previously specified *Pe*, Figure 20 will yield the value of K_{eff} that should be used. From this value, the actual rate of heating, *K*, can be calculated and Figure 19 will give an estimate of the required dimensionless heating time. This will be the shortest heating time available under the above constraints. Notice from Figure 20 that lowering the Peclet number will allow a higher value of K_{eff}, resulting in a lower dimensionless heating time. If it is possible to decrease Peclet number without decreasing velocity, then this should be done, as it would permit fastest heating. However, if the Peclet number is decreased by lowering the velocity, the corresponding increase in K_{eff} and decrease in dimensionless heating time, τ_h^*, will be offset by an increase in actual heating time, τ_h, proportional in magnitude to the decrease in velocity. Therefore, from the perspective of minimizing the total heating time, subject to a constraint of maximum allowable temperature gradient, the higher velocity is always better.

To further illustrate application of the above-described design methodology, consider the following example. Assume the maximum allowable dimensionless temperature gradient is 0.1, and *Pe* = 10. From Figure 20, this gives $K_{eff} = 0.1$, and Figure 19 gives dimensionless heating time of 11. Now, attempt to lower the heating time by lowering airflow velocity. If the velocity is lowered by a factor of 10, then *Pe* = 1, and $K_{eff} \approx 0.2$. This gives a new dimensionless heating time of approximately 6, which is ~45% lower than the original

dimensionless heating time of 11. However, *actual* heating time will not decrease, but *increase* by a factor of 60/11 (or 545%) since it scales inversely proportional to the effective velocity. Clearly, the situation only becomes worse as velocity is decreased further.

Because of the use of properly scaled dimensionless variables, Figures 19 through 21 have the advantage of presenting a large amount of information on a single curve. However, to increase our understanding of the underlying physics of the heating process it is advantageous to refer back to physical parameters in outlining generalized design rules for optimization of the heating/cooling process.

In particular, Figure 22 shows a design map (with dimensional quantities) created from the purely convective model predictions (see Eqs. (46) and (47)). This model was shown in Section 3.3 to be valid over specific ranges of effective Peclet number and effective rate of inlet temperature rise. The map in Figure 22 is specific to the geometry and material selection previously specified (see Figure 14 and Table 3), and considers a unit cell being heated from 25 $^{\circ}C$ to 625 $^{\circ}C$ (the map is applicable for any process involving a 600 $^{\circ}C$ temperature change). Lines of constant K and u are shown with maximum spatial temperature gradient on the vertical axis and heating time on the horizontal axis. Once a horizontal line corresponding to the maximum allowable temperature gradient is specified, K and u can be chosen below that line such that heating time is minimized. This allows some flexibility in choice of K and u but these parameters are likely to be restricted by system constraints such as pumping power, heater size, etc. Alternatively, the maximum allowable heating time could be the specified design constraint, in which case K and u are chosen such that temperature gradient is minimized. This would give an estimate of the allowable

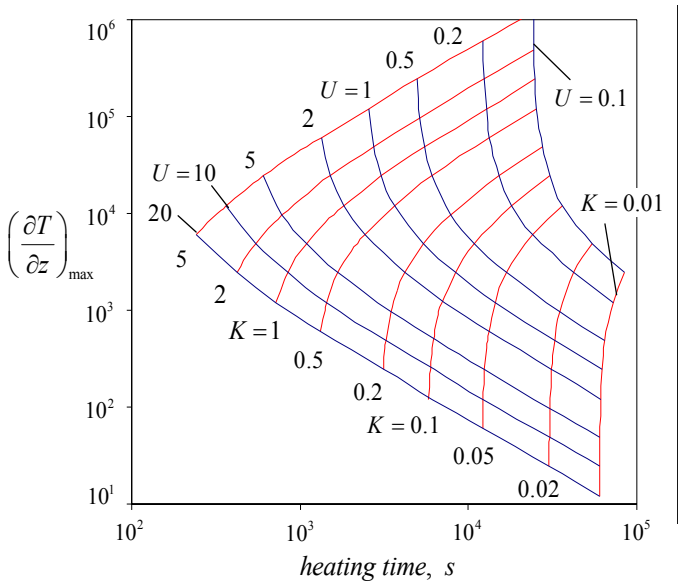

Figure 22. Design map based on purely convective model predictions of spatial temperature gradient (°*C*/*m*) vs. heating time (*s*) for various *K* and *u*. This map is specific to the cell geometry and materials described in Fig. 1 and Table 1, and is applicable to a cell being heated or cooled over a 600 °*C* temperature interval.

gradients that the cell must be designed to withstand if the heating time requirement is to be met. Notice that increasing the air flow speed, *u*, always allows movement in a favorable direction on the map (i.e., reduction in both the heating time and maximum temperature gradients), while increasing *K* yields the mixed result of lowered heating time but increased temperature gradients. A design map such as Figure 22 is thus an excellent graphical representation of how the design space may be efficiently searched to yield approximate values of hot air velocity and heating rate to achieve an optimal design of SOFC transient heating process. Once the parameter *K* and *u* values resulting in optimal transient operation have been obtained, only a minimal amount of highly-intensive CFD computations can be used to yield the detailed information required to complete a thermo-mechanical failure analysis of the cell.

3.5 Conclusions/Future work

Reduced-order transient thermal models of varying complexity have been considered for optimizing the heating and cooling of an SOFC unit cell. The first and most general one—the two-equation, coupled solid-gas model—resulted in fast numerical solution of the problem, compared to CFD simulations, but was shown to be unreliable for predicting maximum temperature gradients. The next two models—the convective-conductive heating and purely convective heating--permitted analytical solutions of the time-varying temperature field in the cell. The simplest of these, the purely convective heating model, also yielded explicit, algebraic relationships between heating time, temperature gradients, hot air velocity, and heating rate. These predictions of integral thermal quantities (i.e., the heating time and maximum spatial and temporal temperature gradients) were shown to be valid for a fairly broad range of operating parameters through comparison with fully 3-D Fluent simulations. The more general convective-conductive model of the cell provided little improvement in accuracy over the purely convective model; however, its formulation and analysis led to the definition of the appropriate scales for physical velocity and the dimensionless parameters that govern cell transient response.

Predictions of the analytical models have been presented in the form of generalized thermal design maps, and a specific example of a design map based on the purely convective model was used to develop a conceptual framework for optimizing a heating and cooling process. Our analysis shows that increasing the velocity of the hot air stream, and lowering the Peclet number (by increasing the effective thermal diffusivity of the cell) leads to the optimal design, which minimizes heating time under the constraint of maximum allowable

temperature gradients. While this result is hardly surprising in hindsight, the ability of the purely convective model to accurately predict favorable design trends with little or no computational effort makes it a powerful tool for searching the design space in the early stages of transient process development.

Throughout the development of these reduced-order models and thermal design maps, it has been assumed that the maximum allowable temperature gradient (to avoid failure of cell components) is known *a-priori* based on thermo-mechanical stress analysis. This is not necessarily the case and efforts similar to [32] are required for the development of relationships between failure, maximum allowable stresses, and maximum allowable temperature gradients as relevant to SOFC transients. Also, the effects of thermal cycling require additional research—in particular quantification of cell lifetime in terms of number of cycles and maximum temperature gradients developed during each cycle. Another assumption of the current analysis that will be challenged is that the cell is perfectly insulated. In reality, the cell heat losses are temperature dependent (increasing as the cell heats up) which raises the possibility that the heating times could be much longer than what has been predicted here. In the most extreme case, a cell might never reach the desired operating temperature if the magnitude of heat input is not sufficiently larger than heat losses. Finally, extension and validation of the current analysis for other geometries, such as cross-flow cells, will greatly expand the applicability of the results. This future work will complement and enhance the presently developed simple and computationally efficient design rules for transient heating/cooling of the SOFC.

CHAPTER 4

LOCAL THERMAL NON-EQUILIBRIUM EFFECTS IN POROUS ELECTRODES

4.1 Introduction

Thermal modeling is a vital tool in the design and development of SOFCs due to the close coupling between temperature, reaction kinetics, ionic resistance of the electrolyte, current density, operating voltage, fuel utilization, and flow fields. Accurate prediction of the temperature fields within SOFCs is not only essential to predicting and optimizing overall cell performance, but is also a prerequisite to mitigating thermo-mechanical degradation and failure of the delicate anode-electrolyte-cathode structure. These concerns have resulted in the development of highly detailed CFD/FEM based models whose ability to predict *global* quantities such as average current density, voltage, and temperature has been well established through experimental validation. However, lack of *detailed* experimental data such as local temperature fields or current density distribution has prohibited a more thorough validation of the numerical models. Thus, simplifying assumptions of the models can and should be challenged from a physical standpoint in order to maintain rigor and to provide the required careful justification (and limits of validity) of those assumptions.

One such assumption is that the temperatures of the gas phase and solid matrix within porous electrodes are locally the same, i.e. the gas and solid are in local thermal equilibrium (LTE). A survey of the relevant literature indicates that most (possibly all) of the current models make this assumption with little or no justification given. (Recently, however, Hwang [40] has addressed this issue in modeling low temperature proton exchange membrane fuel cells.) Three typical conditions found in the porous electrodes of SOFCs

bring the assumption of local thermal equilibrium into question: 1) the presence of volumetric heat generation in the medium, 2) very low Reynolds number flow, and 3) large difference in thermal conductivities of the solid and gas phases. Under these conditions, the gas and solid temperatures can differ greatly and local thermal non-equilibrium (LTNE) modeling is often required [41]. To carefully address these issues, LTNE effects are investigated here through an order of magnitude analysis, which results in the development of a single LTNE parameter that can be used to assess the validity of the local thermal equilibrium assumption in SOFCs.

4.2 Model formulation

During steady state operation, all of the heat generated within the anode-electrolyte-cathode structure of a well-insulated cell is transferred to the fuel and oxidizer flow streams, which carry it out of the cell. In the porous electrodes, most of the heat is generated near the electrode-electrolyte interface (see Figure 23) and is dissipated by (*i*) conduction through the solid matrix, (*ii*) heat transfer from the solid to the gas phase by convection within the porous electrodes, and (*iii*) advection of the gas through the micro-pores of the electrode into the flow channel. These processes are accounted for in the following two-equation, thermal non-equilibrium model, derived from conservation of energy in the gas and solid phases [41]:

$$\begin{aligned} 0 &= \nabla\cdot\left(k_{s,eff}\ \nabla\ T_s\right) + h_{sf}a_s\left(T_f - T_s\right) + \sum\dot{Q}'''_{gen_i} \quad \text{(Solid phase)} \\ \nabla\cdot\left(\rho\ \vec{V}\ c_p\ T_f\right) &= \nabla\cdot\left(k_{f,eff}\ \nabla\ T_f\right) - h_{sf}a_s\left(T_f - T_s\right) \quad \text{(Gas phase)} \end{aligned} \tag{49}$$

where h_{sf} is the solid to gas phase convective heat transfer coefficient, a_s is the specific (per unit volume) surface area within a representative volume of the media, ρ is density, c_p is specific heat, and $\vec{V}$ is velocity of the gas phase, and $\dot{Q}'''_{gen_i}$ represents sources of volumetric

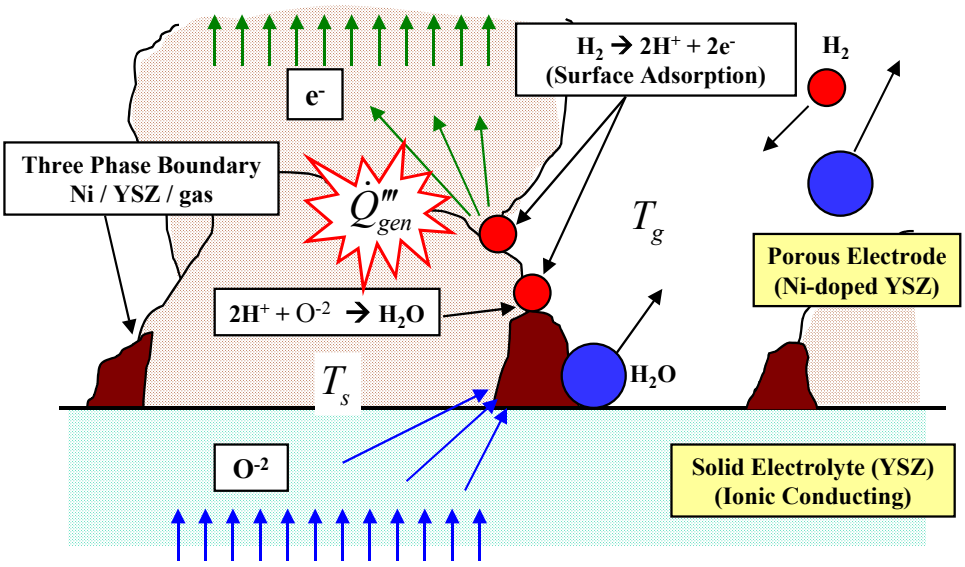

Figure 23. Schematic representation of the TPB region of the porous anode and solid electrolyte of a SOFC. Oxygen ions migrate from the cathode side, through the electrolyte, and react with hydrogen ions adsorbed on the surfaces of the anode to form water vapor. Heat generated due to electrochemical reaction and ohmic losses is dissipated by two mechanisms: convection to the gas phase and conduction through the solid.

heat generation within the solid phase. The simplest models for isotropic effective thermal conductivity of the solid and gas phases are,

$$k_{s,eff} = (1-\varepsilon)k_s; \quad k_{f,eff} = \varepsilon k_f \tag{50}$$

respectively, where ε is porosity.

The magnitude of the difference in local temperatures between the gas and solid phases, $\Delta T = T_s - T_f$, is an indicator of the validity of the assumption of local thermal equilibrium (LTE). Since heat generation is the driving force behind any thermal non-equilibrium in SOFCs, an order of magnitude analysis of the energy conservation equation for the solid phase in Eqs. (49) yields a proper estimate of the magnitude of ΔT. As a first approximation, temperature gradients in the solid (first term on the right-hand-side) can be assumed small compared to the other two terms in the equation and can be neglected. This

requires that the remaining two terms balance each other, and the expected temperature difference is then scaled as,

$$\Delta T \sim \dot{Q}'''_{gen} / h_{sf} a_s \tag{51}$$

This temperature difference is the greatest possible (upper bound) that can be expected for the problem at hand, because it assumes that all the heat generated in the solid is dissipated by convection to the gas phase. For verification, examine the effects of the assumption that the heat conduction term is negligible. As solid conduction effects become significant, this provides an additional route for heat transfer, leading to a reduction in convective heat transfer, and thus, reducing the temperature difference between solid and gas. Therefore, Eq. (51) is a conservative indicator of whether or not LTNE effects should be neglected. The remaining task is to estimate the magnitude of the heat generation term and the interstitial heat transfer coefficient, $h_v = h_{sf} a_s$, that would be expected in the SOFC.

4.3 Scaling analysis

4.3.1 Interstitial heat transfer coefficient

The solid to gas phase heat transfer coefficient, h_{sf}, depends on the thermal conductivity of the fluid, the Reynolds number of the flow, and the geometric characteristics of the medium. The specific surface area, a_s, also depends on the structure of the solid matrix. As a first approximation for this order of magnitude analysis, the structure of the porous electrode material can be assumed isotropic, consisting of roughly spherical particles of diameter, d_p. This is a conservative approximation—more so than considering a continuous solid phase, which would enhance conductive heat transfer, thereby reducing LTNE effects. The SOFC electrodes have pores or voids of diameter, d_v, which has been

experimentally measured as 0.3 – 0.4 μm for anode materials [42]. (For simplicity, we assume that pore size in the cathode is of the same magnitude.) The relationship between specific surface area and void diameter given by Vafai [43] is $a_s = 4\varepsilon / d_v$. This yields a specific surface area of the order of 4×10^6 m^{-1}. Particle diameter can be estimated from the equation for the specific surface area for either spherical particles [44],

$$a_s = 6(1-\varepsilon)/d_p \tag{52}$$

or for sintered metal beads [45],

$$a_s = 20.346(1-\varepsilon)\varepsilon^2/d_p \tag{53}$$

yielding 0.9 and 1.1 μm, respectively. Although the exact value of these parameters is uncertain for the available porous electrode materials, it is clear that a_s is proportional to $1/d_p$, and particle and void diameters are the same order of magnitude.

Another area of uncertainty in determining interstitial heat transfer coefficient is the Reynolds number, $\mathrm{Re}_d = \rho_f u d_p / \mu_f$, of the gas flow through the micro-pores of the electrodes. In general, it is reasonable to expect that the transport through the electrodes, especially near the electrode-electrolyte interface, is dominated by diffusion [42, 46]. In this region, known as the triple phase boundary (TPB) region, the electrochemical reaction takes place at the junction of catalyst, electrolyte and gas phase. As a first estimate, the order of magnitude of the average velocity here can be found from conservation of mass and Faraday's law, which relates moles of reactants or products to electrical current. Specifically, for a given current density, the required mole flux of the relevant species (e.g. H_2) to the TPB is given by, $\dot{n} = i/2F$, where i is the current density of the cell ($A\ m^{-2}$), F is Faraday's constant (96500 $C\ mol^{-1}\ e^{-1}$), and the 2 appears because 2 electrons are produced

by the balanced electrochemical reaction. For a representative current density of 10^4 $A\ m^{-2}$ the corresponding mass flux of H_2 to the TPB region is of the order 0.1 $g\ m^{-2}\ s^{-1}$. Dividing by density and porosity yields a gas phase velocity on the order of 0.01 $m\ s^{-1}$. Given such small velocity and using the previously estimated particle diameter and appropriate fluid properties, it becomes apparent that $\mathrm{Re}_d \ll 1$ in the electrochemically active region of the porous electrode.

A very common correlation for h_{sf}, developed by Wakao and Kaguei [47] from an extensive collection of experimental data (for spherical particles) is,

$$h_{sf} = \frac{k_f}{d_p}\left[2 + 1.1\mathrm{Re}_d^{\,0.6}\,\mathrm{Pr}_f^{\,0.33}\right] \tag{54}$$

where, k_f is the thermal conductivity of the fluid and Pr_f is the Prandtl number of the fluid. This correlation is valid over a large range of Re_d, although little data exists for very low Reynolds numbers. However, the correlation does asymptotically approach the correct theoretical value of h_{sf} in the limit of $\mathrm{Re}_d \to 0$ (pure conduction through the gas phase). (Other frequently used correlations, such as that of Kar and Dybbs [48], do not appear to be valid at this limit [41].) Using the fact that $\mathrm{Re}_d \ll 1$ as previously discussed, Eq. (54) is reduced to,

$$h_{sf} \sim 2k_f / d_p \tag{55}$$

This is the most conservative estimate of h_{sf} since it considers only heat transfer by conduction in the gas. Any increase in Re_d would only increase the heat transfer coefficient from this baseline value.

Combining Eq (55) with Eq. (52) or (53) yields a lower bound estimate of the interstitial heat transfer coefficient, h_v. A typical value of this parameter for air, assuming electrodes with 1 μm particles and porosity of 30% is on the order of 10^{11} $W\,m^{-3}\,K^{-1}$. This very high volumetric heat transfer coefficient is due to efficient heat transfer within the microscale porous structure of the electrodes because of the very large specific surface area. Since the calculations are sensitive to particle diameter and porosity, results will be presented for a range of these parameters.

4.3.2 Volumetric heat generation

An upper limit for the magnitude of the volumetric heat generation term, $\dot{Q}'''_{gen}$ in Eq. (51) is found from an examination of the thermodynamic effects associated with electrochemical reactions in the fuel cell and the ohmic heating effects in the ionic conducting electrolyte material. Although the processes by which heat is generated are complex and coupled, the overall energy balance of the cell effectively provides an estimate of the upper limit of heat generated without requiring an in-depth analysis of these processes. The total heat generation for a single cell can be calculated based on a given current density, and that quantity of heat is then applied to the TPB region (assumed to be a 10 μm thick layer next to the electrolyte [42]) in order to estimate the upper bound of volumetric heat generation.

The reversible electrochemical reaction for the hydrogen-fueled cell [6] is,

$$\mathrm{H_2} + \frac{1}{2}\mathrm{O_2} + 2\mathrm{e^-} \rightleftharpoons \mathrm{H_2O} + 2\mathrm{e^-} \tag{56}$$

The limit of the energy available for electrical work is the Gibbs free energy given by,

$$\Delta G = \Delta H - T\Delta S = -nFE_{ideal} \tag{57}$$

where, n is the number of electrons (2) in Eq. (56), F is Faraday's constant, and E_{ideal} is the ideal reaction potential evaluated at the operating temperature and pressure of the cell. The quantity $T\Delta S$ is the heat generated by the reaction (per mole of hydrogen) if the cell is operating ideally (reversibly) and ΔH is the net enthalpy of formation of products and reactants. Rewriting Eq. (57) in terms of readily available, tabulated values of E^o, G^o, H^o, and S^o at standard conditions (298 K, 1 atm), and assuming H does not vary with temperature ($\Delta H \approx \Delta H^o$) [6], the total reversible heat generated ($kJ\ mol^{-1}$) by the reaction is,

$$Q_{rev} = -T^o \Delta S^o + nF\left(E^o - E_{ideal}\right) \tag{58}$$

where the superscript ^{o} indicates quantities evaluated at standard conditions. From Faraday's law, the *rate* of heat generation on a *volumetric* basis in the solid is,

$$\dot{Q}'''_{rev} = \frac{i}{L(1-\varepsilon)}\left[-\frac{T^o \Delta S^o}{nF} + \left(E^o - E_{ideal}\right)\right] \tag{59}$$

where, i is the current density, L is the length scale (thickness) of the heat generating region, and ε is porosity. Because the cell does not operate ideally, the operating voltage is lower than the ideal voltage. This voltage drop is primarily due to the ionic resistance of the electrolyte, activation overpotential, and concentration overpotential, resulting in additional heat generation which can be calculated as,

$$\dot{Q}'''_{irrev} = \frac{i}{L(1-\varepsilon)}\left(E_{ideal} - E_{oper}\right) \tag{60}$$

Thus, after adding Eqs. (59) and (60), the total volumetric heat generation is expressed as,

$$\dot{Q}'''_{total} = \frac{i}{L(1-\varepsilon)} \cdot \left[-\frac{T^o \Delta S^o}{nF} + \left(E^o - E_{oper}\right)\right] \tag{61}$$

For example, consider a cell operating at $E_{oper} = 0.5\ V$ and a current density of $i = 10^4\ A\ m^{-2}$. For the reaction given in Eq. (56), the standard potential, E^o, is 1.22 V, and $T^o \Delta S^o$ is –48.6 $kJ\ mol^{-1}$ [49]. If all the generated heat is confined to the 10 μm thick TPB region, the volumetric heat source term is of the order $10^9\ W\ m^{-3}$. The large magnitude of this term is a result of the conservative assumption that all heat-generating processes occur in a very small region of the porous electrodes, while in fact they are distributed through the electrodes and electrolyte.

4.4 Estimate of LTNE effects

Having developed expressions for heat generation and interstitial heat transfer coefficient, the LTNE criteria given in Eq. (51) can now be used to estimate the maximum temperature non-uniformity between the solid and gas phases. To consider the case of maximum heat generation, the operating voltage in Eq. (61) is set at zero (i.e., cell is short-

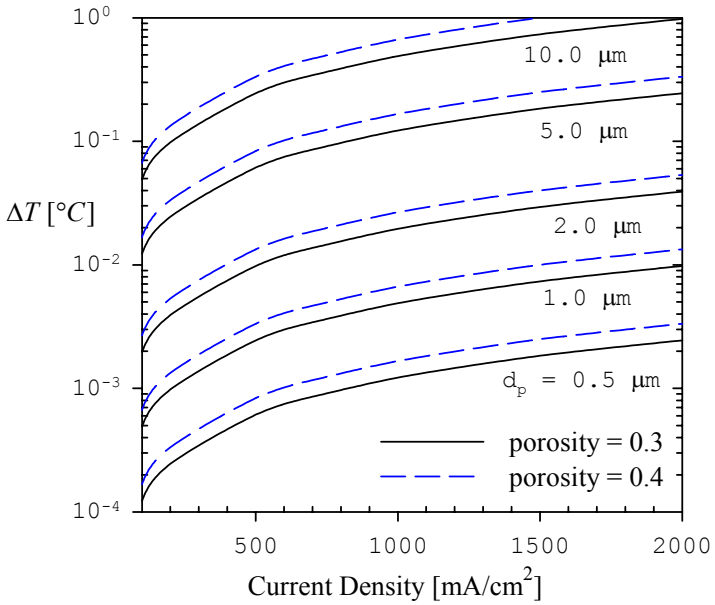

Figure 24. The maximum expected temperature difference between the solid and gas phase of the porous medium as a function of current density for various porosity and particle diameter of the porous electrodes. In this plot the thickness of the heat generating region is assumed to be 10 μm.

circuited and drawing maximum current), and this equation along with Eqs. (52) and (55) are substituted into Eq. (51), yielding an estimate of a maximum gas-to-solid temperature difference that can be expected in SOFC electrodes,

$$\Delta T_{\max} \sim 0.12 \frac{i\, d_p^2}{k_f L (1-\varepsilon)^2} \tag{62}$$

This parameter allows the user to determine if LTNE effects can safely be ignored, or if detailed non-equilibrium thermal modeling is required. Figure 24 shows a plot of $\Delta T_{\max}$ vs. electrode particle diameter for various values of current density. Although our assumptions have erred on the side of maximizing the expected temperature difference, it should be noted that local current density could be significantly higher than the average value used in Eq. (62) leading to local "hot spots" with increased LTNE effects. It is left to the discretion of the user to properly interpret the results of Eq. (62) and use relevant local values of i, k_f, L, and ε in assessing the validity of the LTE assumption for specific cases.

CONCLUSION

Thermo-mechanical failure of components in planar-type solid oxide fuel cells (SOFCs) is a major obstacle on the path to bringing this technology to commercial viability. The probability of material degradation and failure in SOFCs depends strongly on the local temperature gradients at the interfaces of different materials. Therefore, it is of paramount importance to accurately predict and manage the temperature fields within the stack, especially near the interfaces. In this work three effects were considered in great detail.

First, radiative heat transfer effects within the semi-transparent solid electrolyte were analyzed and compared to thermal conduction. Also, the modeling approach for calculation of surface-to-surface exchange within the flow channels and from the stack to the environment was presented. The necessary simplifying assumptions were identified and their carefully justified range of applicability to the problem at hand was established. This work has contributed to overall thermal modeling efforts by allowing thermal radiation effects to be properly included SOFC models with the minimum computational expense requirement.

Second, we developed a framework for optimization of the transient heating and cooling of SOFCs, leading to the optimal design which minimizes heating time while maintaining thermal gradients below an allowable threshold. This was accomplished through the formulation of reduced order transient thermal models (validated by rigorous CFD simulations) that yielded simple algebraic design rules for predicting maximum thermal gradients and heating time requirements. Several governing dimensionless parameters and time scales were identified that shed light on the essential physics of the process.

Finally, an analysis was performed to assess the degree of local thermal non-equilibrium (LTNE) within porous SOFC electrodes, and through a simple scaling analysis we discovered the parameter that gives an estimate of the magnitude of LTNE effects. We conclude that because of efficient heat transfer between the solid and gas in the microscale pores of the electrodes, the temperature difference between gas and solid is often negligible. However, if local variations in current density are significant, the LTNE effects may become significant and should be considered.

APPENDIX A

SOLUTION OF 2-FLUX EQUATION

The 2nd order ODE describing spectral radiative heat flux as a function of spectral optical thickness is,

$$\frac{d^2 q_\lambda}{d\tau_\lambda^2} - (1-\omega_\lambda)(4q_\lambda) \quad = \quad (1-\omega_\lambda)4\frac{dE_{b\lambda}}{d\tau_\lambda} \tag{A.1}$$

subject to the boundary conditions,

$$\begin{aligned} \tau_\lambda = 0: \quad & -\frac{\left(1-\rho_{\lambda,1}\right)}{1-\omega}\frac{dq_\lambda}{d\tau_\lambda} + 2\left(1+\rho_{\lambda,1}\right)q_\lambda = 4\left(\varepsilon_\lambda E_{b\lambda}\right)_1 - \left(1-\rho_{\lambda,1}\right)4\pi I_{b\lambda} \\ \tau_\lambda = \tau_{\lambda,L}: \quad & -\frac{\left(1-\rho_{\lambda,2}\right)}{1-\omega}\frac{dq_\lambda}{d\tau_\lambda} - 2\left(1-\rho_{\lambda,2}\right)q_\lambda = 4\left(\varepsilon_\lambda E_{b\lambda}\right)_2 - \left(1-\rho_{\lambda,2}\right)4\pi I_{b\lambda} \end{aligned} \tag{A.2}$$

These equations are derived from the RTE following the procedure outlined in Chapter 14 of Modest [19]. The homogeneous portion of the solution is,

$$\left(q_\lambda\right)_{\text{hom}} \quad = \quad C_1 \mathrm{e}^{2\sqrt{1-\omega_\lambda}\,\tau_\lambda} + C_2 \mathrm{e}^{-2\sqrt{1-\omega_\lambda}\,\tau_\lambda} \tag{A.3}$$

and the particular solution is,

$$\left(q_\lambda\right)_P = \sqrt{1-\omega_\lambda}\left[e^{2\sqrt{1-\omega_\lambda}\tau_\lambda}\int_0^{\tau_\lambda} e^{-2\sqrt{1-\omega_\lambda}\tau_\lambda'}\frac{dE_{b\lambda}}{d\tau_\lambda'}d\tau_\lambda' - e^{-2\sqrt{1-\omega_\lambda}\tau_\lambda}\int_0^{\tau_\lambda} e^{+2\sqrt{1-\omega_\lambda}\tau_\lambda'}\frac{dE_{b\lambda}}{d\tau_\lambda'}d\tau_\lambda'\right] \tag{A.4}$$

The integrals of blackbody emissive power with respect to optical thickness can be rewritten in a more manageable form after integration by parts, i.e.

$$\int_0^{\tau_\lambda} e^{-2\sqrt{1-\omega}\,\tau_\lambda}\frac{dE_{b\lambda}}{d\tau_\lambda}d\tau_\lambda = E_{b\lambda}e^{-2\sqrt{1-\omega}\,\tau_\lambda} - E_{b\lambda} + 2\sqrt{1-\omega}\int_0^{\tau_\lambda} e^{-2\sqrt{1-\omega}\,\tau_\lambda}E_{b\lambda}d\tau_\lambda \tag{A.5}$$

The constants C_1 and C_2 are found from the boundary conditions. For simplicity, we introduce several new variables as placeholders,

$$A_1 = \left[\left(1+\rho_{\lambda,1}\right) - \frac{\left(1-\rho_{\lambda,1}\right)}{D} \right] \qquad B_1 = \left[\left(1+\rho_{\lambda,1}\right) + \frac{\left(1-\rho_{\lambda,1}\right)}{D} \right]$$

$$A_2 = \left[\left(1+\rho_{\lambda,2}\right) - \frac{\left(1-\rho_{\lambda,2}\right)}{D} \right] e^{-2D\tau_{\lambda,L}} \qquad B_2 = \left[\left(1+\rho_{\lambda,2}\right) + \frac{\left(1-\rho_{\lambda,2}\right)}{D} \right] e^{2D\tau_{\lambda,L}} \tag{A.6}$$

where, $D = \sqrt{1-\omega}$

This allows the constants to be expressed as,

$$C_1 = -\frac{K_1 A_2 + B_1 K_2}{B_1 B_2 - A_1 A_2} \qquad C_2 = \frac{K_2 A_1 + B_2 K_1}{B_1 B_2 - A_1 A_2}$$

where,

$$K_1 = 2\varepsilon_{\lambda,1}\left(E_{b\lambda,1} - E_{b\lambda}\right)$$

$$\begin{aligned} K_2 = {} & 2\varepsilon_{\lambda,2}E_{b\lambda,2} - \left(\varepsilon_{\lambda,2} + D\left(1+\rho_{\lambda,2}\right)\right)\left[e^{2D\tau_{\lambda,L}}E_{b\lambda}\right] \\ & - \left(\varepsilon_{\lambda,2} - D\left(1+\rho_{\lambda,2}\right)\right)\left[e^{-2D\tau_{\lambda,L}}E_{b\lambda}\right] \\ & + \left(\varepsilon_{\lambda,2} + D\left(1+\rho_{\lambda,2}\right)\right)2De^{2D\tau_{\lambda,L}}\int_0^{\tau_{\lambda,L}} e^{-2D\tau_\lambda}E_{b\lambda}d\tau_\lambda \\ & - \left(\varepsilon_{\lambda,2} - D\left(1+\rho_{\lambda,2}\right)\right)2De^{-2D\tau_{\lambda,L}}\int_0^{\tau_{\lambda,L}} e^{2D\tau_\lambda}E_{b\lambda}d\tau_\lambda \end{aligned} \tag{A.7}$$

The integrals in the expression for K_2 can only be evaluated numerically. Total radiative heat flux is found by integrating spectral radiative heat flux over the entire spectrum,

$$\begin{aligned} q = {} & \int_0^\infty C_1 e^{2D\tau_\lambda}d\lambda + \int_0^\infty C_2 e^{-2D\tau_\lambda}d\lambda + \int_0^\infty \left[2D^2 e^{2D\tau_\lambda}\int_0^{\tau_\lambda} e^{-2D\tau_\lambda}E_{b\lambda}d\tau_\lambda \right] d\lambda \\ & + \int_0^\infty \left[2D^2 e^{-2D\tau_\lambda}\int_0^{\tau_\lambda} e^{2D\tau_\lambda}E_{b\lambda}d\tau_\lambda \right] d\lambda - \int_0^\infty De^{2D\tau_\lambda}E_{b\lambda}d\lambda + \int_0^\infty De^{-2D\tau_\lambda}E_{b\lambda}d\lambda \end{aligned} \tag{A.8}$$

The first integral is approximated by discretizing the spectrum into *N* intervals,

$$\int_0^\infty C_1 e^{2D\tau_\lambda}d\lambda = \sum_{i=1}^N \exp\left[2D\left(\tau_\lambda\right)_i\right]\int_{\lambda_i}^{\lambda_{i+1}}\left(C_1\right)d\lambda \tag{A.9}$$

It should be remembered that C_1 and C_2 are spectrally dependent. The second integral is,

$$\int_0^\infty C_2 e^{-2D\tau_\lambda}d\lambda = \sum_{i=1}^N \exp\left[-2D\left(\tau_\lambda\right)_i\right]\int_{\lambda_i}^{\lambda_{i+1}}\left(C_2\right)d\lambda \tag{A.10}$$

The third integral is,

$$\int_0^{\infty}\left[2D^2e^{2D\tau_\lambda}\int_0^{\tau_\lambda}e^{-2D\tau_\lambda}E_{b\lambda}d\tau_\lambda\right]d\lambda$$
$$=2D^2\sum_{i=1}^{N}\left[\exp\left[2D\left(\tau_\lambda\right)_i\right]\sum_{j=1}^{M}\exp\left[-2D\left(\overline{\tau}_\lambda\right)_{i,j}\right]\left(\Delta\tau_\lambda\right)_{i,j}\left(\int_{\lambda_i}^{\lambda_{i+1}}E_{b\lambda}d\lambda\right)_j\right] \tag{A.11}$$

and fourth integral,

$$\int_0^{\infty}\left[2D^2e^{-2D\tau_\lambda}\int_0^{\tau_\lambda}e^{2D\tau_\lambda}E_{b\lambda}d\tau_\lambda\right]d\lambda$$
$$=2D^2\sum_{i=1}^{N}\left[\exp\left[-2D\left(\tau_\lambda\right)_i\right]\sum_{j=1}^{M}\exp\left[2D\left(\overline{\tau}_\lambda\right)_{i,j}\right]\left(\Delta\tau_\lambda\right)_{i,j}\left(\int_{\lambda_i}^{\lambda_{i+1}}E_{b\lambda}d\lambda\right)_j\right] \tag{A.12}$$

and finally the last two integrals are

$$\int_0^{\infty}De^{2D\tau_\lambda}E_{b\lambda}d\lambda+\int_0^{\infty}De^{-2D\tau_\lambda}E_{b\lambda}d\lambda$$
$$=D\sum_{i=1}^{N}\left(\exp\left[2D\left(\tau_\lambda\right)_i\right]+\exp\left[-2D\left(\tau_\lambda\right)_i\right]\right)\int_{\lambda_i}^{\lambda_{i+1}}E_{b\lambda}d\lambda \tag{A.13}$$

APPENDIX B

NUMERICAL SOLUTION OF 2-EQN COUPLED MODEL

The set of coupled partial differential equations describing the two-equation reduced-order transient heating model are

$$\begin{aligned} solid: \quad & \sum_i \left(\rho c_p A\right)_i \frac{\partial T_s}{\partial t} = \sum_i \left(kA\right)_i \frac{\partial^2 T_s}{\partial z^2} + hP_{g-s}\left(T_g - T_s\right) \\ gas: \quad & \left(\rho c_p A\right)_g \left[\frac{\partial T_g}{\partial t} + u\frac{\partial T_g}{\partial z}\right] = \left(kA\right)_g \frac{\partial^2 T_g}{\partial z^2} + hP_{g-s}\left(T_s - T_g\right) \end{aligned} \tag{B.1}$$

with boundary and initial conditions,

$$\begin{aligned} \underline{B.C.'s}: \quad & \frac{\partial T_s}{\partial z}(0,t) = \frac{\partial T_s}{\partial z}(L,t) = 0; \qquad \underline{I.C.}: \quad T_s(z,0) = T_g(z,0) = T_o \\ & T_g(0,t) = f(t) \end{aligned} \tag{B.2}$$

The solid and gas layers are discretized in the following manner:

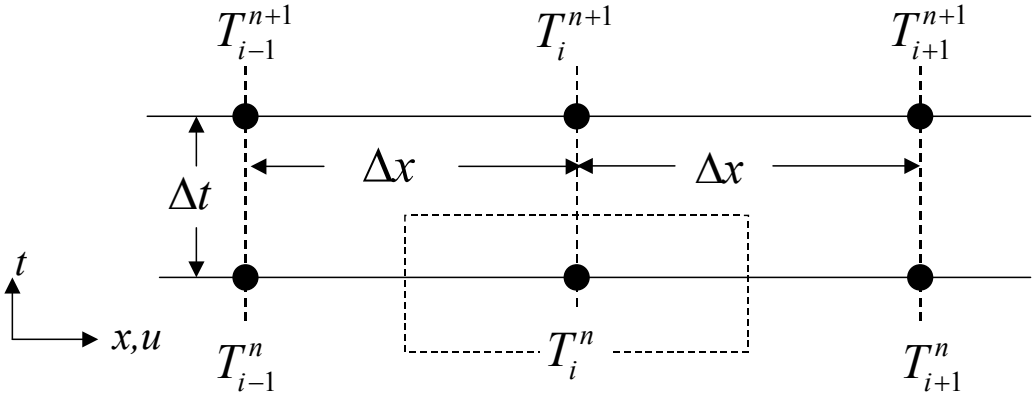

and then applying conservation of energy to each node gives the set of linear algebraic equations for the gas temperature,

$$\begin{aligned} & C_g \frac{T_i^{n+1} - T_i^n}{\Delta t}\Delta x \\ & = \beta\left[k_g \frac{T_{i+1} - 2T_i + T_{i-1}}{\Delta x} + C_g u \frac{T_{i-1} - T_i}{\Delta x}\Delta x - hP_{g-s}\left(T_i - T_{i,s}\right)\Delta x\right]^{n+1} \\ & + (1-\beta)\left[k_g \frac{T_{i+1} - 2T_i + T_{i-1}}{\Delta x} + C_g u \frac{T_{i-1} - T_i}{\Delta x}\Delta x - hP_{g-s}\left(T_i - T_{i,s}\right)\Delta x\right]^{n} \end{aligned} \tag{B.3}$$

where $0 \le \beta \le 1$ is a weighting factor between fully explicit (forward march in time) and fully implicit integration in time. For our calculations the Crank-Nicholson scheme ($\beta = 0.5$) was absolutely stable and provided the second-order approximation in time. The solid temperature equations are of the form,

$$C_s \frac{T_i^{n+1} - T_i^n}{\Delta t} \Delta x = \beta \left[k_s \frac{T_{i+1} - 2T_i + T_{i-1}}{\Delta x} + hP_{g-s} \left(T_{i,g} - T_i \right) \Delta x \right]^{n+1} + (1-\beta) \left[k_s \frac{T_{i+1} - 2T_i + T_{i-1}}{\Delta x} + hP_{g-s} \left(T_{i,g} - T_i \right) \Delta x \right]^{n} \tag{B.4}$$

Note also the following definitions of effective properties,

$$C_g = \left(\rho c_p A \right)_g; \quad k_g = \left(kA \right)_g; \quad C_s = \sum_i \left(\rho c_p A \right)_i; \quad k_s = \sum_i \left(kA \right)_i \tag{B.5}$$

The boundary conditions for the gas yield the following equations at the inlet,

$$\begin{aligned} & C_g \frac{T_1^{n+1} - T_1^n}{\Delta t} \Delta x \\ & = \beta \left[k_g \frac{T_2 - 3T_1 + 2f(t)}{\Delta x} + C_g u \frac{f(t) - T_1}{\Delta x} \Delta x - hP_{g-s} \left(T_1 - T_{1,s} \right) \Delta x \right]^{n+1} \\ & + (1-\beta) \left[k_g \frac{T_2 - 3T_1 + f(t)}{\Delta x} + C_g u \frac{f(t) - T_1}{\Delta x} \Delta x - hP_{g-s} \left(T_1 - T_{1,s} \right) \Delta x \right]^{n} \end{aligned} \tag{B.6}$$

and at the exit,

$$C_g \frac{T_M^{n+1} - T_M^n}{\Delta t} \Delta x = \beta \left[k_g \frac{-T_M + T_{M-1}}{\Delta x} + C_g u \frac{T_{M-1} - T_M}{\Delta x} - hP_{g-s} \left(T_M - T_{M,s} \right) \Delta x \right]^{n+1} + (1-\beta) \left[k_g \frac{-T_M + T_{M-1}}{\Delta x} + C_g u \frac{T_{M-1} - T_M}{\Delta x} - hP_{g-s} \left(T_M - T_{M,s} \right) \Delta x \right]^{n} \tag{B.7}$$

For the solid at the inlet, the boundary equation is expressed as,

$$C_s \frac{T_1^{n+1} - T_1^n}{\Delta t} \Delta x = \beta \left[k_s \frac{T_2 - T_1}{\Delta x} + hP_{g-s} \left(T_{1,g} - T_1 \right) \Delta x \right]^{n+1} + (1-\beta) \left[k_s \frac{T_2 - T_1}{\Delta x} + hP_{g-s} \left(T_{1,g} - T_1 \right) \Delta x \right]^{n} \tag{B.8}$$

and at the exit,

$$C_s \frac{T_M^{n+1} - T_M^n}{\Delta t} \Delta x = \beta \left[k_s \frac{T_{M-1} - T_M}{\Delta x} + hP_{g-s} \left(T_{M,g} - T_M \right) \Delta x \right]^{n+1} + (1-\beta) \left[k_s \frac{T_{M-1} - T_M}{\Delta x} + hP_{g-s} \left(T_{M,g} - T_M \right) \Delta x \right]^{n} \tag{B.9}$$

The set of equations (B.3) through (B.9) can be written in matrix form as,

$$\begin{aligned} &gas: \\ &\quad [\mathbf{C}_1]\mathbf{T}_g^{n+1} = \lambda_1 \mathbf{T}_s^{n+1} + [\mathbf{C}_2]\mathbf{T}_g^{n} + \lambda_2 \mathbf{T}_s^{n} = \mathbf{r} \\ &solid: \\ &\quad [\mathbf{C}_3]\mathbf{T}_s^{n+1} = \lambda_3 \mathbf{T}_g^{n+1} + [\mathbf{C}_4]\mathbf{T}_s^{n} + \lambda_4 \mathbf{T}_g^{n} = \mathbf{r} \end{aligned} \tag{B.10}$$

where, **T**, is a temperature vector, **C**, is a tri-diagonal coefficient matrix, and λ's are constants.

The procedure for solving the matrix equations (B.10) is as follows:

1. populate the coefficient matrices
2. guess the temperature in the solid for the future time step
3. calculate the right hand side of the gas equation
4. calculate the future temperature in the gas using the tri-diagonal matrix algorithm
5. using the results of the previous step (4), calculate the right hand side of the solid equation
6. calculate the future temperature in the solid using the tri-diagonal matrix algorithm
7. compare the results of the previous step (6) to the guess used in step (2).
8. repeat steps (2) – (7) using the calculated solid temperature as the new guess in step (2) until convergence is obtained.
9. proceed to the next time step and return to step (1).

The best initial guess for step (2) is the solid temperature at the current time step.

APPENDIX C

ANALYTICAL SOLUTION OF TRANSIENT CONVECTIVE-CONDUCTIVE MODEL

We seek a solution of the dimensionless governing equation of the convective-conductive model,

$$\frac{\partial T}{\partial t}+\frac{\partial T}{\partial z}=\frac{1}{Pe}\frac{\partial^2 T}{\partial z^2} \tag{C.1}$$

subject to the boundary and initial conditions,

$$\begin{aligned} &T(0,t)-\beta\frac{\partial T}{\partial z}(0,t)=F(t); \quad \left.\frac{\partial T}{\partial z}\right|_{z=1}=0 \\ &T(z,0)=0 \end{aligned} \tag{C.2}$$

where $\beta = 1/Pe$ if diffusion in the gas equation is neglected. We expect the solution to take the form,

$$T(z,t)=\theta(z,t)\cdot e^{Az+Bt} \tag{C.3}$$

where A and B are arbitrary constants found by substituting back into Eq. (C.1). It can be shown that if $A = Pe/2$ and $B = -Pe/4$ then Eq. (C.1) becomes,

$$\frac{\partial \theta}{\partial t}=\frac{1}{Pe}\frac{\partial^2 \theta}{\partial z^2} \tag{C.4}$$

The boundary and initial conditions of the original problem are transformed yielding,

$$\begin{aligned} &\frac{1}{2}Pe\cdot\theta(0,t)-\frac{\partial\theta}{\partial z}(0,t)=Pe\cdot F(t)\cdot e^{-Bt}=f(t) \\ &\frac{1}{2}Pe\cdot\theta(1,t)+\frac{\partial\theta}{\partial z}(1,t)=0; \quad \theta(z,0)=0 \end{aligned} \tag{C.5}$$

The problem is complicated by the presence of a *non-homogeneous, time-dependent* boundary condition. Assume the problem described by Eqs. (C.4) and (C.5) can be expressed as,

$$\theta(z,t)=\theta^*(z,t)+D_1(t)\cdot z+D_2(t) \tag{C.6}$$

where the unknown functions are found by forcing the boundary conditions to be homogeneous yielding,

$$D_1(t) = \frac{-2}{4+Pe} f(t); \qquad D_2(t) = \frac{4+2Pe}{Pe(4+Pe)} f(t) \tag{C.7}$$

Thus, Eq. (C.6) becomes,

$$\theta(z,t) = \theta^*(z,t) + \frac{4+2Pe-2Pe\cdot z}{Pe(4+Pe)} f(t) \tag{C.8}$$

with $f(t)$ described by Eq. (C.5) and initial condition,

$$\theta^*(z,0) = -\frac{4+2Pe-2Pe\cdot z}{Pe(4+Pe)} f(0) \tag{C.9}$$

Taking the derivatives of Eq. (C.8) and substituting them into (C.4) yields,

$$\begin{aligned} &\theta_t^*(z,t) = \frac{1}{Pe}\theta_{zz}^*(z,t) - \frac{1}{Pe}S(z,t) \\ &where \quad S(z,t) = \frac{4+2Pe-2Pe\cdot z}{(4+Pe)} f'(t) \end{aligned} \tag{C.10}$$

which can now be solved analytically. The homogeneous portion of Eq. (C.10) is solved using separation of variables,

$$\theta^*(z,t) = Z(z)\Psi(t) \tag{C.11}$$

resulting in the following eigenvalues problem in space,

$$Z'' + \lambda^2 PeZ = 0 \tag{C.12}$$

whose eigenvectors are,

$$\sin(\omega_n z) + \frac{2\omega_n}{Pe}\cos(\omega_n z) \quad n = 1,2,3... \tag{C.13}$$

with the eigenvalues $\omega_n = \lambda_n\sqrt{Pe}$ satisfying the following characteristic equation

$$\cos(\omega_n) + \frac{Pe^2 - 4\omega_n^2}{4\omega_n Pe}\sin(\omega_n) = 0 \tag{C.14}$$

which must be solved numerically.

Next, assume a solution of the form,

$$\theta^*(z,t) = \sum_{n=1}^{\infty} C_n(t)\left[\sin(\omega_n z) + \frac{2\omega_n}{Pe}\cos(\omega_n z)\right] \tag{C.15}$$

where,

$$C_n(t) = \frac{\int_0^1 \theta^*(z,t)\left[\sin(\omega_n z) + \frac{2\omega_n}{Pe}\cos(\omega_n z)\right]dz}{\int_0^1 \left[\sin(\omega_n z) + \frac{2\omega_n}{Pe}\cos(\omega_n z)\right]^2 dz} \tag{C.16}$$

The denominator is the norm, which we will call G_n for now. The next step is to write an ODE for C_n,

$$\frac{dC_n}{dt} = \frac{1}{G_n}\int_0^1 \frac{d\theta^*}{dt}(z,t)\left[\sin(\omega_n z) + \frac{2\omega_n}{Pe}\cos(\omega_n z)\right]dz \tag{C.17}$$

which, from Eq. (C.10) can be rewritten as,

$$\begin{aligned}\frac{dC_n}{dt} = &\frac{1}{G_n Pe}\int_0^1 \frac{d^2\theta^*}{dz^2}(z,t)\left[\sin(\omega_n z) + \frac{2\omega_n}{Pe}\cos(\omega_n z)\right]dz \\ &-\frac{1}{G_n Pe}\int_0^1 S(z,t)\left[\sin(\omega_n z) + \frac{2\omega_n}{Pe}\cos(\omega_n z)\right]dz\end{aligned} \tag{C.18}$$

The first integral on the RHS is integrated by parts twice, and after some manipulations, it can be shown that,

$$\begin{aligned}\frac{dC_n}{dt} = &-\frac{\lambda_n^2}{G_n}\int_0^1 \theta^*(z,t)\left[\sin(\omega z) + \frac{2\omega}{Pe}\cos(\omega z)\right]dz \\ &-\frac{1}{G_n Pe}\int_0^1 S(z,t)\left[\sin(\omega z) + \frac{2\omega}{Pe}\cos(\omega z)\right]dz\end{aligned} \tag{C.19}$$

or, more conveniently,

$$\frac{dC_n}{dt} + \lambda_n^2 C_n = -\frac{1}{G_n Pe}\int_0^1 S(z,t)\left[\sin(\omega z) + \frac{2\omega}{Pe}\cos(\omega z)\right]dz \tag{C.20}$$

The solution of this ODE is found using an integrating factor, $e^{\int \lambda^2 dt}$, with solution,

$$C_n(t) = C_n(0)e^{-\lambda_n^2 t} - e^{-\lambda_n^2 t}\frac{1}{G_n Pe}\int_0^t e^{\lambda_n^2 \tau}\int_0^1 S(z,\tau)\left[\sin(\omega_n z)+\frac{2\omega_n}{Pe}\cos(\omega_n z)\right]dz\,d\tau \tag{C.21}$$

where,

$$C_n(0) = \frac{1}{G_n}\int_0^1 \theta^*(z,0)\left[\sin(\omega_n z)+\frac{2\omega_n}{Pe}\cos(\omega_n z)\right]dz \tag{C.22}$$

The integrals for G_n, $C_n(0)$, and $S(z,\tau)$ are now evaluated. For the inlet temperature specified as a linear function of time,

$$F(t) = \frac{T_o + K^*\left(L/u_{eff}\right)t^* - T_o}{T_f - T_o} = K_{eff}t$$
$$f(t) = Pe\cdot F(t)e^{-Bt} = \boxed{Pe\cdot K_{eff}t\cdot e^{\frac{Pe}{4}t}} \tag{C.23}$$

Also, note that once the inlet temperature function reaches the final temperature at time t_1, the inlet temperature is held constant at T_f and the function becomes,

$$t > t_1 \qquad f(t) = Pe\cdot e^{\frac{Pe}{4}t} \quad where, \quad t_1 = \frac{1}{K_{eff}} \tag{C.24}$$

Because $f(0) = 0$, then $C_n(0) = 0$ and G_n's are constant,

$$G_n = \frac{1}{2\omega_n Pe^2}\left[\begin{array}{l}\left(2\omega_n{}^2 - \frac{1}{2}Pe^2\right)\sin(2\omega_n) \\ -2\omega_n Pe\left(\cos(2\omega_n)-1\right)+4\omega_n{}^3 + Pe^2\omega_n\end{array}\right] \tag{C.25}$$

Next, the integral,

$$C_n(t) = -e^{-\lambda_n^2 t}\frac{1}{G_n Pe}\int_0^t e^{\lambda_n^2 \tau}\int_0^1 S(z,\tau)\left[\sin(\omega_n z)+\frac{2\omega_n}{Pe}\cos(\omega_n z)\right]dz\,d\tau \tag{C.26}$$

First, the interior,

$$\int_0^1 S(z,\tau)\left[\sin(\omega_n z)+\frac{2\omega_n}{Pe}\cos(\omega_n z)\right]dz$$
$$= f'(t)\int_0^1 \frac{4+2Pe-2Pe\cdot z}{(4+Pe)}\left[\sin(\omega_n z)+\frac{2\omega_n}{Pe}\cos(\omega_n z)\right]dz \qquad \text{(C.27)}$$
$$= \frac{2}{\omega} f'(t)$$

Next, the outer integration,

$$\frac{2}{\omega}\int_0^t e^{\lambda_n^2\tau} f'(\tau)\,d\tau = \frac{2}{\omega}\int_0^t e^{\left(\lambda_n^2+\frac{Pe}{4}\right)\tau}\left[PeK+\frac{1}{4}Pe^2(K\tau)\right]d\tau$$
$$= \frac{2PeK}{\omega\left(4\lambda_n^2+Pe\right)^2}\left[\left(16\lambda_n^2+Pe^2t+4Pe\lambda_n^2 t\right)e^{\left(\lambda_n^2+\frac{Pe}{4}\right)t}-16\lambda_n^2\right] \qquad \text{(C.28)}$$

So,

$$C_n(t) =$$
$$\frac{2K}{G_n\omega\left(4\lambda_n^2+Pe\right)^2}\left[\left(16\lambda_n^2+Pe^2t+4Pe\lambda_n^2 t\right)e^{\frac{Pe}{4}t}-16\lambda_n^2 e^{-\lambda_n^2 t}\right] \qquad \text{(C.29)}$$

Finally, the integration for the final, constant portion of the inlet temperature function,

$$t > t_1$$
$$\frac{2}{\omega}\int_0^t e^{\lambda_n^2\tau} f'(\tau)\,d\tau =$$
$$\frac{Pe^2}{2\omega}\int_{t_1}^t e^{\left(\lambda_n^2+\frac{Pe}{4}\right)\tau}d\tau = \frac{2Pe^2}{\omega\left(4\lambda_n^2+Pe\right)}\left[e^{\left(\lambda_n^2+\frac{Pe}{4}\right)t}-e^{\left(\lambda_n^2+\frac{Pe}{4}\right)t_1}\right] \qquad \text{(C.30)}$$
$$C_n(t) = -\frac{2Pe}{\omega G_n\left(4\lambda_n^2+Pe\right)}\left[e^{\frac{Pe}{4}t}-e^{\lambda_n^2(t_1-t)+\frac{Pe}{4}t_1}\right]$$

REFERENCES

[1] J.-B.J. Fourier, "Mémoire sur les Températures du Globe Terreste et des Espaces Planétaires", Mémoirs d l'Académie Royale des Sciences de l'Institute de France, **VII** (1827) 570-604. Translation by R. T. Pierrehumbert, "Warming the world", Nature, **432** (2004) 677 (*online supplemental material*)

[2] D.L. Damm and A.G. Fedorov, "Spectral radiative heat transfer analysis of the planar SOFC", Journal of Fuel Cell Science and Technology, **2** (2005) 258-262

[3] D.L. Damm and A.G. Fedorov, "Radiation heat transfer in SOFC materials and components", Journal of Power Sources, **143** (2005) 158-165

[4] D.L. Damm and A.G. Fedorov, "Reduced-order transient thermal modeling for SOFC heating and cooling", Journal of Power Sources, in review, October 2005

[5] D.L. Damm and A.G. Fedorov, "Local thermal non-equilibrium effects in the porous electrodes of the hydrogen-fueled SOFC", Journal of Power Sources, in review, September 2005

[6] *Fuel Cell Handbook*, 5th ed. EG&G Services, National Technical Information Service, U.S. Dept. of Commerce, 2000

[7] A. Hirano, M. Suzuki, M. Ippommatsu, "Evaluation of a new solid oxide fuel cell system by non-isothermal modeling", Journal of the Electrochemical Society, **139** (10) (1992) 2744-2751

[8] S. Ahmed, C. McPheeters, R. Kumar, "Thermal-hydraulic model of a monolithic solid oxide fuel cell", Journal of the Electrochemical Society, **138** (9) (1991) 2712-2718

[9] N. F. Bessette, W. J. Wepfer, "Mathematical model of a tubular solid oxide fuel cell", *Thermodynamics and the Design, Analysis, and Improvement of Energy Systems*, ASME AES pub. **27** (1992) 69-8

[10] J. Hartvigsen, S. Elangovan, A. Khandkar, "Modeling, desing, and performance of solid oxide fuel cells", *Proceedings, Science & Technology of Zirconia V*, (1993) 682-693

[11] S. Murthy and A.G. Fedorov, "Radiation heat transfer analysis of the monolith type solid oxide fuel cell", Journal of Power Sources, **124** (2003) 453-458

[12] J.D.J. VanderSteen and J.G. Pharoah, "The role of radiative heat transfer with participating gases on the temperature distribution in solid oxide fuel cells", *Proceedings, Fuel Cell Science, Engineering, and Technology,* ASME, Rochester, NY, (2004) 483-490

[13] P.W. Li, L. Schaefer, M.K. Chyu, "A numerical model coupling the heat and gas species' transport processes in a tubular SOFC", Journal of Heat Transfer, **126** (2004) 219-229

[14] C. Haynes and W.J. Wepfer, "Characterizing heat transfer within a commercial-grade tubular solid oxide fuel cell for enhanced thermal management", International Journal of Hydrogen Energy, **26** (2001) 369-379

[15] H. Yakabe, T. Ogiwara, M. Hishinuma, I. Yasuda, "3-D model calculation for planar SOFC", Journal of Power Sources, **102** (2001) 144-154

[16] A.C. Burt, I.B. Celik, R.S. Gemmen, A.V. Smirnov, "A numerical study of cell-to-cell variations in a SOFC stack", Journal of Power Sources, **126** (2004) 76-87

[17] M. Spinnler, E.R.F. Winter, R. Viskanta, "Studies on high-temperature multilayer thermal insulations", International Journal of Heat and Mass Transfer, **47** (2004) 1305-1312

[18] M. Spinnler, E.R.F. Winter, R. Viskanta, "Theoretical studies of high-temperature multilayer thermal insulations using radiation scaling", Journal of Quantitative Spectroscopy & Radiative Transfer, **84** (2004) 477-491

[19] M.F. Modest, *Radiative Heat Transfer*, 2nd Ed., Academic Press, New York, 2003

[20] M. Varady and A.G. Fedorov, "Combined radiation and conduction in glass foams", Journal of Heat Transfer, **124** (2002) 1103-1110

[21] M.T. Prinkey, R.S. Gemmen, W.A. Rogers, "Application of a new CFD analysis tool for SOFC technology", *Proceedings, International Mechanical Engineering Congress and Exposition*, ASME, HTD **369**-4 (2001) 291-300

[22] W.A. Rogers, R.S. Gemmen, C. Johnson, M. Prinkey, M. Shahnam, "Validation and Application of a CFD-based model for solid oxide fuel cells and stacks", *Proceedings, Fuel Cell Science, Engineering, and Technology,* ASME, Rochester, NY, (2003) 517-520

[23] N. Autissier, D. Larrain, J. Van herle, D. Favrat, "CFD simulation tool for solid oxide fuel cells", Journal of Power Sources, **131** (2004) 313-319

[24] M.A. Khaleel, Z. Lin, P. Singh, W. Surdoval, D. Collin, "A finite element analysis modeling tool for solid oxide fuel cell development: coupled electrochemistry, thermal, and flow analysis in MARC®", Journal of Power Sources, **130** (2004) 136-148

[25] A.L. Boehman, "Radiation heat transfer in catalytic monoliths", AIChE Journal, **44** (12) (1998) 2745-2755

[26] N.S. Kaisare, J.H. Lee, A.G. Fedorov, "Hydrogen generation in a reverse-flow microreactor: 1. Model formulation and scaling", AIChE Journal, 51 (8) (2005) 2254-2264

[27] X. Fu, R. Viskanta, J.P. Gore, "Combustion and heat transfer interaction in a pore-scale refractory tube burner", Journal of ThermoPhysics and Heat Transfer, **12** (2) (1998) 164-171

[28] H. Lee and R.O. Buckius, "Reducing scattering to nonscattering problems in radiation heat transfer", International Journal of Heat and Mass Transfer, **26** (1983) 1055-1062

[29] H. Lee and R.O. Buckius, "Combined mode heat transfer analysis utilizing radiation scaling", High Temp-High Pressures, **17** (1985) 626-632

[30] L. Petruzzi, S. Cocchi, F. Fineschi, "A global thermo-electrochemical model for SOFC systems design and engineering", Journal of Power Sources, **118** (2003) 96-107

[31] M. Iwata, T. Hikosaka, M. Morita, T. Iwanari, K. Ito, K. Onada, Y. Esaki, Y. Sakaki, S. Nagata, "Performance analysis of planar-type unit SOFC considering current and temperature distributions", Solid State Ionics, **132** (2000) 297-308

[32] A. Selimovic, M. Kemm, T. Torisson, M. Assadi, "Steady state and transient thermal stress analysis in planar solid oxide fuel cells", Journal of Power Sources **145** (2005) 463-469

[33] G. Hawkes, J. O'Brien, C. Stoots, S. Herring, M. Shahnam, "Thermal and electrochemical three dimensional CFD model of a planar solid oxide electrolysis cell", *Proceedings, ASME Summer Heat Transfer Conference*, HT2005, San Francisco, CA, July 17-22, 2005

[34] C.L. Haynes and J.C. Ford, "A simulation of the solid oxide fuel cell electrochemical 'light-off' phenomenon", *Proceedings, ASME Summer Heat Transfer Conference*, HT2005, San Francisco, CA, July 17-22, 2005

[35] D.L. Damm and A.G. Fedorov, "Simplified thermal analysis of the SOFC transients during startup/shutdown", *Proceedings, ASME Summer Heat Transfer Conference*, HT2005, San Francisco, CA, July 17-22, 2005

[36] W.H. Press, S.A. Teukolsky, W.T. Vetterling, B.P Flannery, *Numerical Recipes in C*, second ed., Cambridge University Press, New York, 1995

[37] S. Kakac, R.K. Shah, W. Aung, *Handbook of Single-Phase Convective Heat Transfer*, Wiley & Sons, New York, 1987

[38] J. Sucec, "Exact solution for unsteady conjugated heat transfer in the thermal entrance region of a duct", Journal of Heat Transfer, **109** (1987) 295-299

[39] A.G. Fedorov and R. Viskanta, "Three dimensional conjugate heat transfer in the microchannel heat sink for electronic packaging", International Journal of Heat and Mass Transfer, **43** (2000) 399-415

[40] J.J. Hwang, "Heat transfer in a porous cathode of fuel cells", *Proceedings, ASME Summer Heat Transfer Conference*, HT2005, San Francisco, CA, July 17-22, 2005

[41] M. Kaviany, *Principles of Heat Transfer in Porous Media*, 2nd ed., Springer-Verlag New York Inc., 1995

[42] R.E. Williford, L.A. Chick, S.P. Simner, G.D. Maupin, J.W. Stevenson, "Diffusion limitations in the porous anodes of solid oxide fuel cells", Journal of the Electrochemical Society, **150** (8) (2003) A1067-A1072

[43] K. Vafai, *Handbook of Porous Media*, Marcel Dekker, 2000

[44] F.A.L. Dullien, *Porous Media Fluid Transport and Pore Structure*, Academic Press, New York, 1979

[45] G. J. Hwang and C.H. Chao, "Heat transfer measurement and analysis for sintered porous channels", Journal of Heat Transfer, **116** (1994) 456-464

[46] J. Yuan, M. Rokni, B. Sunden, "Three-dimensional computational analysis of gas and heat transport phenomena in ducts relevant for anode-supported solid oxide fuel cells", International Journal of Heat and Mass Transfer, **46** (2003) 809-821

[47] N. Wakao and S. Kaguei, *Heat and Mass Transfer in Packed Beds*, Gordon & Breach, New York, 1982

[48] K.K. Kar and A. Dybbs, "Internal heat transfer coefficients of porous metals", *Proceedings, ASME Winter Annual. Meeting*, Phoenix, AZ, (1982) 81-91

[49] M.J. Moran, H.N. Shapiro, *Fundamentals of Engineering Thermodynamics*, 4th ed. Wiley & Sons, Inc., New York, 2000